Ketamine triggers a switch in excitatory neuronal activity across neocortex

Joseph Cichon[1,2], **Andrzej Z. Wasilczuk**[1], **Loren L. Looger**[3], **Diego Contreras**[2], **Max B. Kelz**[1,4], **Alex Proekt**[1,4]

[1]Department of Anesthesiology and Critical Care, Perelman School of Medicine, University of Pennsylvania, Philadelphia, PA, USA.

[2]Department of Neuroscience, Perelman School of Medicine, University of Pennsylvania, Philadelphia, PA, USA.

[3]Janelia Research Campus, Howard Hughes Medical Institute, Ashburn, VA, USA.

[4]Mahoney Institute for Neurosciences, Perelman School of Medicine, University of Pennsylvania, Philadelphia, PA, USA.

Abstract

The brain can become transiently disconnected from the environment while maintaining vivid, internally generated experiences. This so-called 'dissociated state' can occur in pathological conditions and under the influence of psychedelics or the anesthetic ketamine (KET). The cellular and circuit mechanisms producing the dissociative state remain poorly understood. We show in mice that KET causes spontaneously active neurons to become suppressed while previously silent neurons become spontaneously activated. This switch occurs in all cortical layers and different cortical regions, is induced by both systemic and cortical application of KET and is mediated by suppression of parvalbumin and somatostatin interneuron activity and inhibition of NMDA receptors and HCN channels. Combined, our results reveal two largely non-overlapping cortical neuronal populations–one engaged in wakefulness, the other contributing to the KET-

induced brain state–and may lay the foundation for understanding how the brain might become disconnected from the surrounding environment while maintaining internal subjective experiences.

The dissociated state, defined loosely as a detachment from reality with varying degrees of intensity and duration, can naturally occur during severe stress, trauma, psychiatric disorders, epileptic episodes or reliably ensue after pharmacological treatment with psychedelics or the dissociative anesthetic ketamine (KET). KET, traditionally considered an *N*-methyl-D-aspartate receptor (NMDAR) antagonist, remains the key dissociative agent in the clinical practice of anesthesia[1] and the archetypal rapid-acting antidepressant in psychiatry[2]. Subhypnotic KET alters cognition in a manner consistent with psychosis– for example, paranoia, loose associations, tangentiality and unusual thought content[3]. With increasing doses, individuals experience considerable perceptual effects, including alterations of body/environment/time perception, derealization, depersonalization, sensory/ visual illusions and hallucinations. These perceptual effects are paralleled by characteristic electroencephalographic (EEG) signatures consisting of slow oscillations punctuated by bursts of higher-frequency gamma waves[4-6]. The appearance of this EEG signature coincides with individuals failing to respond to sensory inputs[7]. Upon recovery from KET, individuals typically recall vivid perceptual experiences completely divorced from their surrounding environment[8,9]. KET's unique ability to reliably create such vivid experiences while suppressing sensory input processing gave rise to the term 'dissociative anesthetic'.

There has been considerable interest in elucidating the cellular and neural circuit mechanisms of KET's effects over wide dose ranges, with profound clinical and scientific implications. Dissociative experiences in humans and dissociative-like behavior in rodents likely involve the activation of deep postero-medial area of cortex[10]. At the cellular level, subhypnotic doses of KET (also referred to as antidepressant doses) acutely increase glutamatergic transmission[11,12], post-synaptic responses[13] and pyramidal cell firing[14,15]. Over longer time scales, subhypnotic KET induces synaptic plasticity[16,17] in many brain regions. On the molecular level, the effects of KET have been linked to activity-dependent blockade of NMDARs[18] and, to a lesser extent, its modulation of hyperpolarization-activated cyclic-nucleotide-gated (HCN) channels[10,19]. Alterations of a complex, highly interconnected network of GABAergic cortical interneurons may also contribute to KET's effects. For example, fast-spiking parvalbumin (PV)-expressing and somatostatin (SST)-expressing interneurons are rapidly inhibited both by KET and by specific NMDAR antagonists[13,14,20]. Reduced firing of both PV interneurons that target the peri-somatic regions of pyramidal cells[21] and SST interneurons that inhibit their dendrites[22] may underlie KET's pro-excitatory actions on pyramidal neurons via disinhibition. Other interneuron subtypes, such as vasoactive intestinal peptide (VIP)-expressing interneurons, may further promote disinhibition, given their regulation of both PV and SST cells if engaged by KET[23]. It is unclear how these diverse neuronal cell types might respond to doses of KET that elicit a profound disconnection from the surrounding environment and associated sensory stimuli. Furthermore, the neuronal circuit mechanisms contributing to KET-induced dissociation remain unknown.

By imaging across different cortical layers and regions in mice in vivo, we show that KET, over a range of subhypnotic doses, induces a rapid switch in spontaneously active pyramidal neuron populations across the neocortex–neurons normally active during wakefulness are suppressed, whereas previously inactive neurons become activated. This activity switch is accompanied by widespread attenuation of cortical inhibition. PV and SST interneuron suppression is necessary for the activity switch. Combined cortical inhibition of NMDAR and HCN channels is sufficient to recapitulate both the neuronal activity switch in primary somatosensory cortex and behavioral features of a KET-induced brain state. Our findings reveal changes in cortical networks that are critical for understanding non-ordinary brain states triggered by KET as well as the relationship between sensory stimuli and likely their subjective perception.

KET induces a switch in the active layer 2/3 neurons

To investigate the neuronal mechanisms contributing to non-ordinary brain states triggered by KET, we used two-photon calcium imaging to record the neuronal activities of excitatory pyramidal neurons in the neocortex of mice before and during KET (Fig. 1a,e). To behaviorally define KET-induced disconnection from the surrounding environment, we first explored a dose range of intraperitoneal (i.p.) KET (single injection) on behaviors in tail suspension test (TST)[24]. Typically, in TST, mice display escape behaviors (swinging and curling movements) and, hence, spend a significant fraction of time mobile. After administration of 50 mg kg^{-1} of KET, these behaviors were eliminated (Fig. 1c, top). During TST, mice exhibited a dose-dependent sustained vertical (as opposed to side-to-side rotational) head-twitching behavior–a characteristic response to psychedelic drugs in rodents[25] (Fig. 1c, bottom, and Supplementary Movie). Mice injected with either 50 mg kg^{-1} or 100 mg kg^{-1} KET also buried fewer marbles in the marble-burying test[26], had an increased time to complete removal of adhesive tape (TAR) from the snout[27] and were less likely to withdraw their forelimb in response to an air puff (failed forelimb withdrawal (FFW)) (Fig. 1d and Extended Data Fig. 1), indicating impaired sensorimotor processing. Although KET reduced these various behaviors, it did not cause marked sedation or gross inhibition of animal movement (Extended Data Fig. 1). Furthermore, these behavioral effects were transient, returned to baseline at ~1 hour and were similar in duration at both 50 mg kg^{-1} and 100 mg kg^{-1} doses when longitudinally tracked (Fig. 1j and Extended Data Fig. 1).

KET administration reduced EEG slow-wave activity compared to wakefulness, without affecting high-frequency oscillations (Fig. 1b and Supplementary Fig. 1), suggesting that the cortex remains highly active. This lends further credence to the assertion that diminished sensorimotor behaviors cannot be explained by sedation. Given that KET produces a dissociative state with similar EEG signatures in humans[4,28], and KET-injected mice became unresponsive to non-painful sensory stimuli while exhibiting a head-twitching phenotype, these results cumulatively suggest that a single injection of KET in mice induces a state with some essential behavioral and neurophysiological similarities to a dissociative-like state in humans.

We first examined the spontaneous calcium activities of pyramidal neurons in cortical layer 2/3 (L2/3) of the forelimb primary somatosensory cortex (S1)[29] during the transition from

wakefulness to the KET-induced state (Fig. 1a,e). GCaMP6f was specifically expressed in excitatory neurons (including L2/3 pyramidal neurons) by taking advantage of transgenic mice expressing GCaMP6-fast (GCaMP6f) under the *Thy1* promoter[30], where neuronal calcium responses could be reliably recorded over time (Supplementary Fig. 2). Most imaging sessions were acquired within 10–20 minutes after KET injection, a timepoint coinciding with peak behavioral features of disconnection (from surrounding environment in TST and impaired sensorimotor processing in TAR and FFW) (Fig. 1c,d and Extended Data Fig. 1). In awake head-restrained mice, S1 pyramidal neurons displayed spontaneous calcium activity under quiet wakefulness, which were categorized into low (0–3 transients per 2 minutes; 69% of cells), moderate (4–6 transients per 2 minutes; 14% of cells) and high (7 transients per 2 minutes; 17% of cells) groups (Fig. 1f,g, saline trace/plot at left). The same regions were reimaged after KET injection based on blood vessel maps, cortical depth, cell morphology and co-expression of a reference fluorescent protein (Supplementary Fig. 2). We found that L2/3 pyramidal neurons underwent rapid and persistent changes in spontaneous activity: highly active neurons became less active or inactive under KET (dose range from 50 mg kg^{-1} to 150 mg kg^{-1}), whereas a subset of neurons that were inactive or weakly active during wakefulness became activated (Fig. 1f,g, Supplementary Fig. 2 and Extended Data Fig. 2). This somatic activity reconfiguration was also present in their output signals as measured by imaging their boutons in cortical layer 1 (Extended Data Fig. 2). Lower doses of KET or conventional anesthetics that lack dissociative properties did not elicit this reconfiguration of neuronal activity in L2/3 (Extended Data Figs. 2 and 3). The effect of KET at doses 50, 100 and 150 mg kg^{-1} was strongly negatively correlated with baseline activity during wakefulness (Fig. 1h and Extended Data Fig. 2). The absolute difference in calcium transients of individual neurons across brain states, referred to as the activity switch index (ASI), was significantly greater in the KET-treated mice than in saline-injected controls (Fig. 1i). In a subset of animals, we obtained imaging and TAR behavior data simultaneously. This revealed that changes in ASI paralleled changes in behavioral performance in KET-treated mice but not in saline controls (Fig. 1j). It should be noted that an elevated ASI captures cells with increasing, decreasing or switching activity profiles. Thus, ASI simply reflects a change in neuronal activity induced by KET. A non-parametric permutation test, by contrast, provides quantitative evidence for the conclusion that KET induces a switch in L2/3 neuronal activity (Extended Data Fig. 4). The switch in neuronal activity of L2/3 pyramidal neurons is best appreciated when considering scatter plots, ASI and permutation tests.

Despite the emergence of this neuronal activity switch, KET preserved or even increased (at 50 mg kg^{-1} KET) the overall average spontaneous rate of L2/3 transients across all neurons (without sorting or regard to their activity type before or after KET) relative to saline controls (Fig. 1k). The peak amplitude (F/F$_0$) was maintained with KET at 50 mg kg^{-1} but reduced after 100 mg kg^{-1} (Fig. 1l). Additionally, KET did not impact all L2/3 neurons, as ~20–30% of all neurons remained silent across both wakefulness and KET. These results suggest that KET at 50 mg kg^{-1} and 100 mg kg^{-1} induced a brain state with features of disconnection from surrounding environment and impairments in sensorimotor processing, and this brain state is accompanied by a rapid and persistent switch of L2/3 pyramidal cell activity in S1.

Input and output cortical layers undergo activity switch

To determine whether this neuronal switch was restricted to L2/3, we imaged and analyzed the activity of neurons in layer 4 (L4), an input recipient layer, and layer 5 (L5), an output layer, again using *Thy1*-GCaMP6f mice. Both L4 and L5 neurons also displayed a KET-induced rapid and persistent switch of neuronal activity, with highly active cells becoming less active or inactive under KET, and inactive or weakly active cells under wakefulness becoming activated (Fig. 2a,c for L4 and Fig. 2b,g for L5; Extended Data Fig. 5). This reconfiguration of activity was reflected in a significant increase in ASI for both layers compared to saline controls (Fig. 2d for L4 and Fig. 2h for L5). Like L2/3, the overall average spontaneous rate (without sorting or regard to their activity type before or after KET) and peak responses of L4 and L5 transients were maintained between KET and saline controls (Fig. 2e,f for L4 and Fig. 2i,j for L5). L4 and L5 responses remained stable after saline injection (Extended Data Fig. 5). Taken together, these data suggest that KET suppresses highly active neurons under wakefulness and activates a subset of inactive excitatory neurons. This acute switch in the active population of neurons occurs across all layers within S1.

KET-induced switch in active L2/3 neurons across neocortex

To determine if this activity switch is a general phenomenon that occurs across diverse cortical regions, we imaged and analyzed the neuronal activity of L2/3 neurons in another sensory region (primary visual cortex (V1)), a neighboring motor region (forelimb primary motor cortex (M1)), and two association areas (secondary motor cortex (M2) and retrosplenial cortex (RS)) with KET at both doses (Fig. 3a and Extended Data Fig. 6). In all imaged regions, KET suppressed the activity of highly active neurons under wakefulness and activated inactive neurons (Fig. 3a-c and Extended Data Fig. 6). KET at both doses induced a significant increase in L2/3 ASI relative to saline-injected controls (Fig. 3c and Extended Data Fig. 6). These experiments suggest that KET induces a switch in the active population of excitatory neurons across the neocortex.

Neuronal activity switch arises locally in cortical circuits

KET affects neurons throughout the brain. Thus, it is possible that the observed effects of KET on cortical activity are due to its effect on subcortical nuclei[31,32] or the thalamus[33]. To address these possibilities, we performed L2/3 imaging before and after local delivery of ~1 μl of KET to the cortex through a small bone hole lateral to the S1 imaging region at concentrations (50 μM and 500 μM), similar to those previously used to study local KET-associated cortical responses[34]. KET diffused, on average, ~500 μm into the S1 region during the 20-minute recording session and, thus, was largely confined to the cortex (Fig. 4a and Supplementary Fig. 3). Local KET administration at both concentrations induced a switch in L2/3 activity (Fig. 4b-d). Local KET injection increased the ASI of L2/3 neurons as compared to artificial cerebrospinal fluid (aCSF) control-injected mice (local KET at 50/500 μM: 3.3 ± 0.3 / 3.2 ± 0.3 versus aCSF-injected control: 1.6 ± 0.2, Kruskal–Wallis: $P < 0.001$ for both concentrations). The proportion of cells with increasing or decreasing activity induced by local KET injection was similar to that of systemic KET (Fig. 4b; local

KET: increasing 43%, no change 13%, decreasing 44% versus systemic KET: increasing 38%, no change 21%, decreasing 41%). Thus, systemic (Fig. 1) or local KET is sufficient to induce the rapid switch in the active population of neurons within S1.

KET activates a subset of silent neurons, whereas other silent neurons remain unaffected (Figs. 1f–h and 4b–d). It is possible that, although both systemic and local KET elicit a neuronal switch, each switch involves distinct neuronal populations. To address this possibility, we followed the same L2/3 neurons through systemic KET (50 mg kg^{-1}) and then local KET (50 μM) administration on the following day (Fig. 4e). The effect of systemic KET on L2/3 neurons was strongly positively correlated ($r = 0.67$, $P = 7.7 \times 10^{-8}$) with the effect of local KET on the following day, indicating that KET is modulating (activating or inhibiting) a specific subset of neurons, whereas other neighboring neurons remain unaffected (Fig. 4e). This KET-specific modulation of L2/3 activity was also induced with repeated administrations of systemic KET but not with saline injections (Fig. 4f,g). These experiments imply that both systemic and local KET affect similar neuronal subpopulations and that the KET-induced neuronal switch is reproducible in similar neuronal populations.

Because systemic and local KET induce a significant neuronal switch in largely the same population of S1 neurons, we wondered whether a neuronal switch confined to S1 might be sufficient to induce behavioral features of a dissociative-like state as measured by TAR. To test this possibility, we analyzed the animals' performance on TAR before and after local KET or aCSF delivery to bilateral S1 or V1 as a control (Fig. 4h, cartoon depicting KET/aCSF delivery sites). Bilateral delivery of local KET to S1 was sufficient to significantly impair the animal's performance as compared to bilateral aCSF injections to S1 or local KET delivered to V1 (Fig. 4h). These results suggest that local KET administration recapitulates the effects of systemic KET both on cortical microcircuit activity and behavior. Thus, we hypothesize that the changes in cortical neuronal activity observed under systemic KET (Figs. 1-3) are likely related to KET's specific local modulation of inputs, interneuronal connections and/or post-synaptic molecular targets directly affecting neurons in the neocortex.

Pyramidal activity switch requires PV and SST suppression

Different interneuron subtypes target specific domains of pyramidal neurons and other local interneurons, providing precise spatiotemporal control of excitatory and inhibitory outputs and cortical dynamics. Subhypnotic, antidepressant doses of KET are thought to alter pyramidal neuron activity through specific modulation of GABAergic interneurons–for example, PV-expressing and SST-expressing populations[13,20,35]. To investigate the role of interneurons in the KET-induced neuronal switch of pyramidal neurons, we first explored spontaneous activity of the various groups of interneurons residing in S1 with systemic administration of KET at 50 mg kg^{-1} and 100 mg kg^{-1} as well as after local KET delivery (50 μM). By taking advantage of several interneuron-specific Cre driver lines coupled with Cre-dependent adeno-associated virus (AAV) to exclusively express GCaMP6f in these cell types, we were able to examine the activity profiles of the major interneurons groups in this region (Fig. 5a; cartoon depicts interneuron circuitry in S1) (see Methods for details).

Here, we found that both systemic and local doses of KET, but not saline injection, induce a generalized suppression of the spontaneous rate and peak response across all interneuron subtypes from baseline measures taken in wakefulness (Fig. 5b-e and Extended Data Fig. 7). This reduction in the spontaneous rate and peak response of interneuron calcium activity is in striking contrast to their neighboring pyramidal cells, which generally maintain their signals during this state transition (Figs. 1k,l and 2e,f,i,j). Like subhypnotic dosing of KET, KET at 50 mg kg^{-1} and 100 mg kg^{-1} and local KET (50 μM) induce profound reductions in the neuronal activities among several genetically diverse groups of cortical interneurons.

To determine if this reduction in interneuron activity is required for the neuronal switch in L2/3 excitatory pyramidal neurons (Fig. 5f), we attempted to prevent the KET-induced suppression of interneuron activity by activating them autonomously using a chemogenetic approach. To increase S1 interneuron activity in vivo, we specifically transfected Cre-expressing interneuron subtypes with an AAV encoding Cre-dependent hM$_3$D(G$_q$) designer receptor exclusively activated by designer drug (DREADD) receptor (Extended Data Fig. 8)[36]. Binding of the ligand clozapine *N*-oxide (CNO) to hM$_3$D(G$_q$) receptors activates G$_q$-coupled signaling, leading to membrane depolarization and increased firing of target cells through multiple mechanisms, including inhibition of KCNQ channels, enhanced release of internal calcium stores and facilitated coupling between calcium and action potential generation. CNO delivered by i.p. injection to mice expressing hM$_3$D(G$_q$) specifically in SST, PV and VIP cells induced more than two-fold increase in spontaneous calcium activity in wakefulness (Fig. 6a). This activation of interneuron activity was maintained in the presence of KET (Fig. 6a). We next activated these interneuronal subtypes individually before systemic (Fig. 6b) or local (Fig. 6c) KET administration while monitoring the neuronal activity of L2/3 pyramidal neurons across KET treatment. CNO-induced activation of either SST or PV interneurons prevented the KET-induced activity switch in pyramidal neurons (Fig. 6b,c, top two sets of traces, and plots in Fig. 6d), as also indicated by the reduction in the ASI in L2/3 pyramidal neurons in these conditions (Fig. 6e, pink and blue bars). By contrast, activation VIP neurons by CNO did not prevent the KET-induced activity switch (Fig. 6b,c, bottom set of traces, and plot in Fig. 6d). CNO-injected control mice expressing AAV-*synapsin-1*-tdTomato exhibited a strong L2/3 pyramidal neuronal switch after systemic KET (Fig. 6e and Extended Data Fig. 8). The occlusion of the KET-induced switch in L2/3 pyramidal neurons could be mimicked by dose-dependent pharmacologic enhancement of GABA$_A$-R activity in S1 via local midazolam delivery (Extended Data Fig. 9). These experiments suggest that KET-induced reductions in PV and SST neuronal activity are necessary for L2/3 pyramidal neurons to undergo their activity switch. Conversely, although VIP cells are also largely downregulated under KET, the ~10–15% that remain active under KET likely maintain or potentially promote the neuronal switch of L2/3 neurons (Figs. 5d and 6b-e).

Given that the L2/3 neuronal switch tracks with impaired performance on the TAR task (Fig. 1j), we reasoned that an interneuron-induced blockade of the KET-induced activity switch in L2/3 neuron could potentially restore performance on TAR task. To address this possibility, we serially monitored TAR at baseline, after CNO injection and then after systemic or local KET injection in Cre-expressing interneuron mice transfected with AAV encoding Cre-dependent hM$_3$D(G$_q$) (Fig. 6f). CNO-induced activation of SST and PV by itself did not

affect TAR performance, whereas VIP activation induced a mild, yet significant, impairment in TAR as compared to control mice expressing AAV-*synapsin-1*-tdTomato (Fig. 6f, blue shaded region denoted CNO treatment). Systemic KET (50 mg kg^{-1}) after interneuron activation (all subtypes) significantly impaired TAR, but this impairment in performance was no different than control mice (Fig. 6f, left panels). By contrast, the effect of local KET injection on TAR performance was reduced by prior SST or PV interneuron activation but not by prior VIP interneuron activation (Fig. 6f, right panels). Taken together, these data suggest that KET-induced downregulation of SST and PV interneuron activity is not only necessary for the activity switch in L2/3 pyramidal neurons but also contributes to deficits in sensorimotor processing, a behavioral feature of dissociative-like states.

Inhibition of NMDARs or HCN channels drives a switch

Systemic KET has effects on interneurons (Figs. 5 and 6), neuromodulators and multiple post-synaptic receptors and channels that may underlie the neuronal switch in pyramidal neurons (Fig. 7a)[1,10,19]. To investigate whether KET's effects on receptors and channels contribute to the KET-induced activity switch, we modulated various known molecular targets of KET action in vivo with either agonists or specific inhibitors. We found that inhibition of either NMDAR function or HCN activity, via local delivery of MK801 or ZD7288, induced a significant increase in the ASI of L2/3 neurons (Fig. 7b-d). Local MK801 at 100 μM or 500 μM induced a switch-off (a 60–80% suppression of L2/3 activity suppression and a reduction in peak response), whereas local ZD7288 at 100 μM or 500 μM induced a switch-on (54–71% increase in L2/3 activity) (Fig. 7b-e). In either case, the increase in the ASI was not significantly different from that of local KET (Fig. 7d). Modulation of other potential KET molecular targets–including inhibition of nicotinic acetylcholine receptors (mecamylamine at 100 μM) and L-type calcium channels (nifedipine at 100 μM), or activation of opioid signaling (fentanyl at 0.3 mg kg^{-1} i.p.) and enhanced release of endogenous catecholamines (ephedrine at 20 mg kg^{-1} i.p.)–did not induce an activity switch in L2/3 neurons (Fig. 7d,e and Extended Data Fig. 10). These findings suggest that suppression of NMDARs on active neurons and blockade of HCN channel activity on silent neurons can each mimic the ketamine-induced activity switch in pyramidal neurons. Newly activated neurons or those with persistent activity in the presence of NMDAR blockade (by KET or MK801) are driven by AMPA receptor (AMPAR) activity, as their activity is highly sensitive to the AMPAR and kainate receptor blocker DNQX (Extended Data Fig. 10).

NMDAR and HCN channel inhibition recapitulate KET's effects

Next, we blocked NMDAR and HCN channel function simultaneously in vivo via local delivery of both MK801 and ZD7288 inhibitors. Combined blockade of NMDAR and HCN channel function produced an increase in L2/3 ASI; the proportions of cells undergoing increases and decreases in activity were similar to those observed after systemic or local KET delivery (Fig. 8a-d versus Fig. 4). To determine if KET and pharmacological blockade of NMDAR and HCN channel function induce similar activity modulations in local neuronal populations, we sequentially imaged L2/3 neurons initially exposed to systemic KET (50 mg kg^{-1}) and, on the following day, in the presence of local inhibitors (100 μM) (Fig. 8e).

We observed a strong positive correlation between the effect of KET on day 1 and the effect of NMDAR and HCN channel inhibition on the following day (Fig. 8f). We then investigated whether this local drug-induced neuronal switch could drive behavioral features characteristic of KET exposure (like that of Figs. 1d, 4h and 6f). To this end, we bilaterally inhibited NMDAR function (MK801), HCN channel activity (ZD7288) or both in either S1 (experimental) or V1 (control) and monitored the animal's performance on TAR. Bilateral local administration of both inhibitors to S1 impaired TAR performance compared to single inhibitors or controls (Fig. 8g), indicating that behavioral features of a KET-induced brain state may require both the suppression of previously active neurons and the activation of previously silent neurons (Fig. 8h).

Discussion

How the brain generates internal experiences disconnected from the surrounding world is unclear. We demonstrate that subhypnotic doses of KET produce a substantial reorganization of spontaneous neocortical activity—previously active neurons become preferentially suppressed, whereas a subset of previously silent neurons become activated. This switch in the active population of excitatory neurons is observed across different cortical layers of the somatosensory region and across other primary sensory (vibrissal and visual), motor and association areas (M2 and RS) in the neocortex. We identified KET-induced attenuation of SST and PV interneuron activity as necessary and combined inhibition of NMDAR and HCN channel function as sufficient components for driving a neuronal activity switch. Collectively, this switch in the active population of excitatory neurons provides a novel neuronal and circuit understanding of KET's effects in inducing non-ordinary states of consciousness and may explain how KET can disconnect sensory cues from cognitive or affective processing.

The dissociative state is a subjective experience. As such, it is difficult to experimentally characterize, especially in rodents. However, there do appear to be gross behaviors that are characteristically observed in rodents under the influence of psychedelic drugs. Specifically, head-twitching behavior has been established over decades of research as a behavioral marker of the psychedelic state in rodents[25]. In this study, we provide clear behavioral evidence that mice exposed to 50 mg kg^{-1} i.p. KET exhibit continuous vertical (as opposed to rotational, side-to-side) head-twitching behavior when held in tail suspension (Fig. 1c and Supplementary Movie). Together with additional deficits in sensorimotor processing-for example, in tests of air puff withdrawal, adhesive removal (AR) and marble burying (Fig. 1d and Extended Data Fig. 1)–these behaviors provide further evidence that the chosen 50 mg kg^{-1} i.p. dose of KET elicits a non-ordinary brain with classic features of dissociation. A recent study by Vesuna et al. used the same dose of KET in mice[10]. They observed that KET induced a ~1–3-Hz oscillation in neuronal activity. Remarkably, a similar type of activity arises in a human patient whose seizure prodromal symptoms manifest as dissociation. Although it is difficult to directly assess the state of dissociation in rodents, this suggests that the neurophysiological activity in the human brain during naturally occurring dissociation shares essential similarities with that elicited by KET 50 mg kg^{-1} i.p. in rodents. Our characterization of the neuronal activity switch and the circuit mechanisms that contribute to it reveals a novel neurophysiological feature of the KET-induced brain

states, with potential implications for understanding how the brain gives rise to vivid sensory experienced divorced from physical reality.

The nominal dose of KET used in rodent work is significantly higher than that used in clinical settings. There are, however, key differences in how KET is administered to humans and to rodents that complicate the direct comparison of nominal KET doses across species. Both in our study and in that by Vesuna et al., KET was introduced via injection into the peritoneal cavity. This injection creates a depot that slowly releases the drug into the bloodstream. A similar KET administration paradigm is regularly used in humans without intravenous access. When dosed intramuscularly in humans, the nominal KET dose required to attain the same clinical end point is 2–5 times higher that of the intravenous route[37]. In addition to pharmacokinetic differences, there may also be differences in KET metabolism, elimination and target affinity and sensitivity between rodents and humans. The confluence of behavioral and neurophysiological evidence suggests that 50 mg kg^{-1} i.p. KET elicits a non-ordinary brain state that has resemblance to a dissociative-like state in rodents.

KET is thought to preserve subcortical and thalamic activity while altering cortical processing when given systemically at subhypnotic and hypnotic doses[38]. Several lines of evidence argue that KET's behavioral effects stem from neocortical mechanisms. We show that (1) the neuronal switch of spontaneous activity in L4 (thalamic input layer) was similar to those observed in L2/3 and L5 (Fig. 2); (2) local KET application to the cortex was sufficient to produce a neuronal switch (Fig. 4b-e); (3) local KET application modulates neuronal activity in a similar way as systemic KET administration when a local population is followed over time (Fig. 4e); and (4) local KET application impairs performance on a sensorimotor task, and this effect is remarkably similar to that observed after systemic KET (Fig. 4h versus Fig. 1d). Thus, it appears that the neurophysiological and behavioral effects induced by KET are, to a large degree, cortical phenomena. The divergence of cortical activity from thalamic inputs may explain why sensory experiences (altered perception or even sensory/somatic hallucinations) during KET-induced dissociation are unrelated to sensory inputs. Future studies should examine whether the KET-induced activity switch applies equally to spontaneous and stimulus-evoked activities in cortical neurons.

Subhypnotic KET has profound effects on the structure and function of GABAergic interneurons, and these effects seem to be required for KET's antidepressant response[13,17,35]. Accumulating evidence suggests that KET induces a suppression of SST and PV interneuron activities, causing the disinhibition of pyramidal neurons[20], a finding that supports earlier work that NMDAR antagonists initially regulate the spontaneous firing of GABAergic interneurons over pyramidal neurons [39,40]. We found that higher nominal doses of KET maintain this disinhibition circuit motif, as evidenced by a rapid and uniform suppression of spontaneous neuronal activities across three major interneuron subtypes in the S1 with systemic (50 mg kg^{-1} and 100 mg kg^{-1}) and local (50 μM) delivery of KET (Fig. 5 and Extended Data Fig. 7). Meanwhile, pyramidal neurons maintain or increase their net activity (Figs. 1-4). Chemogenetic activation of SST or PV activity patterns blocks the KET-induced neuronal switch in L2/3, whereas activation of VIP interneurons, which regulate SST interneurons and a fraction of PV interneurons[23], did not affect the KET-induced neuronal switch in L2/3 (Fig. 6b-e). Interestingly, the restoration of SST or

PV activity significantly improved performance on TAR when KET was delivered locally as opposed to systemically (Fig. 6f). This blockade of neuronal activity switch coupled with enhanced performance on TAR suggest a link between the KET-induced activity switch and behaviors associated with a KET-induced state of disconnection. We suspect that the reason why chemogenetic activation of SST or PV interneurons did not rescue TAR performance after systemic KET treatment (in contrast to local KET) is that systemic KET administration causes neuronal activity switches in interconnected circuits upstream and downstream to the S1 region.

At the molecular level, KET acts primarily through inhibition of open (or active) NMDARs[18], although many other molecular interactions could underlie its neuronal effects and drive its clinical utility[1] (Fig. 7a). This preferential block of active NMDARs is thought to specifically inhibit areas of cortical pyramidal hyperactivity in models of depression and chronic pain[41,42]. Consistent with these findings, local cortical application of MK801, a more potent and selective open NMDAR antagonist, produced a silencing effect on highly active L2/3 neurons in wakefulness, with only a mild impairment in performance on a sensorimotor task (Figs. 7b-d and 8g). Cortical inhibition of HCN channels, another molecular target of KET[19], drove a net activation of L2/3 neurons, including previously silent neurons, but again failed to fully recapitulate KET's effects at the cellular and behavioral levels. By contrast, simultaneous inhibition of NMDAR and HCN channel function recapitulated both the neuronal activity switch in L2/3 neurons and behavioral effects observed after KET administration (Fig. 8g).

Based on these observations, we propose a working model in which two interrelated phenomena combine to produce the hallmark neuronal switch induced by KET that drives the KET-associated non-ordinary brain state: suppression of previously active neurons and activation of previously silent neurons (Fig. 8h). KET-mediated blockade of highly active NMDAR-dependent synapses impairs dendritic integration, suppressing active pyramidal neurons and interneurons. Various genetically defined GABAergic interneuron types are highly sensitive to KET over a wide range of doses (Fig. 5)[13,20]. In previously silent pyramidal neurons, reduced GABAergic inhibition coupled with HCN channel inactivation enhances the summation of AMPAR-dependent synaptic responses, thus increasing the neuronal firing of those neurons[43,44]. Consistent with this hypothesis, application of an AMPAR blocker silences newly KET-activated neurons, suggesting that these KET-actived neurons likely use AMPAR neurotransmission in lieu of NMDARs (Extended Data Fig. 10). The net result is that cortex deemphasizes NMDAR synapses and potentiates weaker AMPAR synaptic connections, driving new, complex patterns of activity in neurons typically dormant during wakefulness and largely independent of thalamic inputs.

Methods

GCaMP6 expression in mice

All mice were maintained at the University of Pennsylvania Perelman School of Medicine John Morgan animal facility with controlled temperature and humidity conditions and had free access to food and water. All animal handling was in accordance with guidelines set forth by the School of Medicine's Institutional Animal Care and Use Committee (approved

protocol no. 807237). The genetically encoded calcium indicator GCaMP6f was used for calcium imaging of pyramidal cells and interneurons in the cortex. *Thy1*-GCaMP6f (GP5.17; Jackson Laboratory, 025393) readily labels excitatory pyramidal neurons in L2/3, L4 and L5 (ref. [30]). These transgenic mice were used for somatic recordings in all figures except Fig. 5. In Fig. 5, GCaMP6f expression was driven using recombinant AAV in *PV*-IRES-Cre (Jackson Laboratory, 008069), *Sst*-IRES-Cre (Jackson Laboratory, 013044) and *VIP*-IRES-Cre (Jackson Laboratory, 010908) mice. Before AAV infection, mice were genotyped for the presence of Cre based on established protocols. For interneuron-Cre-positive mice, Cre-dependent GcaMP6f was expressed with AAV under the human *synapsin-1* promoter (AAV1-*hSyn1*-Flex-GcaMP6f; $>1 \times 10^{13}$ viral genomes per milliliter (vg ml^{-1}); Addgene, 100833-AAV1). In Supplementary Fig. 2, we used an AAV encoding GcaMP6f and the red fluorescent protein mRuby2 to drive expression of both proteins in the same cell (AAV1-*h5yn1*-mRuby 2-GSG-P2A-GcaMP6f; $>1 \times 10^{13}$ vg ml^{-1}; Addgene, 50943-AAV1). In general, 100 nl of AAV virus was diluted 4–5× in aCSF and injected (Picospritzer; 20 p.s.i., 12 ms per pulse, 1 Hz) over 10–15 minutes at a depth of 300 μm into right S1 using a glass microelectrode immediately lateral to the imaging location (details below).

Acute interneuron activation was accomplished with expression of Cre-dependent DREADD-hM3D(G$_q$) under the human *synapsin-1* promoter in Cre-positive mice (AAV1-*hSyn1*-DIO-hM3D(G$_q$); $>7 \times 10^{12}$ vg ml^{-1}; Addgene, 44361-AAV1). For validation of interneuron activation (DREADD-hM3D(G$_q$)) in vivo (Fig. 6a), two viruses (AAV1-*hSyn1*-Flex-GcaMP6f and AAV1-*hSyn1*-DIO-hM3D (G$_q$)-mCherry) were mixed at equal volumes and injected into the S1 of Cre-positive mice, and interneuron subtype activity was imaged before and 20 minutes after CNO i.p. injection. In experiments where interneurons were activated and pyramidal cells were imaged (Fig. 6b-e), AAV1-*hSyn1*-DIO-hM3D(G$_q$)-mCherry was mixed with AAV1-*hSyn1*-GcaMP6f, and AAVs were injected into interneuron-specific Cre-positive mice. Mice were also injected with AAV1-*hSynapsin1*-tdtTomato in *Thy1*-GcaMP6f to serve as a control for these series of experiments where interneurons were activated and pyramidal cells were imaged (AAV1-*hSyn1*-tdtTomato; $>1 \times 10^{12}$ vg ml^{-1}; Addgene, 104060).

AAV injections were performed in 1.5-month-old mice and subsequently prepared for head fixation and imaging after 2 weeks of AAV expression. Mice were group-housed in temperature-controlled rooms on a 12-hour light/dark cycle after injections. Mice were imaged at 2 months of age, using both sexes for experiments.

Surgical preparation before in vivo imaging

In preparation for imaging, mice underwent a surgical procedure to attach a head holder mount and create an imaging window for two-photon microscopy[45]. In brief, mice were anesthetized with a mixture of 100% oxygen at 2 L min^{-1} and 1.2% isoflurane. A heating pad was used to maintain the animal's body temperature at approximately 37 °C. The mouse's head was shaved, and its skull surface was exposed with a midline scalp incision. The periosteal tissue over the skull surface was removed without damaging the temporal and occipital muscles. A head holder consisting of two parallel metal bars was attached to the

animal's skull to help restrain the animal's head and reduce motion-induced artifacts during imaging. Mice were checked for expression by two-photon imaging through a thinned-skull technique under anesthesia before the cranial window was implanted. In Cre-positive mice injected with AAV, less than 2% of mice were negative for GCaMP fluorescence, suggesting that genotyping error or off-target injection was an uncommon event. If mice were negative for GCaMP expression, mice were euthanized and not used in this study. If positive for GCaMP, a small skull region (~2 mm in diameter) located over the region of interest (ROI) (stereotactic coordinates in mm relative to bregma and midline: S1: −0.1, +2; barrel cortex: −1.1, +3.4; M1: 0, +1.2; V1: 2.6, +2.6; RS: −2, +1; M2: +1.5, +0.3) was removed, and a round glass coverslip (approximately the same size as the bone being removed) was affixed to the skull with Loctite 495. Precaution was taken not to cover the center of glass with dental acrylic cement.

Upon recovering from surgical anesthesia, mice with head mounts were habituated daily (two sessions of 30 minutes with 15-minute break) starting on postoperative day 1 in a custom-built body support to minimize potential stress effects of head restraining and imaging. No obvious distress was observed in habituated animals during imaging experiments. Mice tolerated surgery and stress related to the perioperative period as indicated by a 0–10% drop in weight. Imaging experiments were started on postoperative day 3 after window implantation.

On the day of imaging, awake mice were positioned in the custom head holder device under the two-photon microscope. In vivo two-photon imaging was performed with an Olympus FluoView 1000 two-photon system (tuned to 920 nm) equipped with a Ti:Sapphire laser (Mai Tai DeepSee, Spectra Physics). We minimized KET-induced head twitching by head (secured metal head bars) and body (with a plastic sleeve) restraint on the imaging platform. Mice were head-restrained and imaged for <1 hour in total, imaging across several regions in L2/3 or across cortical layers. Mice received one dose of KET per experimental condition (only exception was in Figs. 4 and 8) because of the potential interference of KET metabolites on neuronal activity and potentially rapid forms of plasticity. In Figs. 4 and 8, where the same mice were re-imaged the following day, the mice were placed back in their home cage with unlimited access to food and water. Pyramidal neurons and interneurons in cortical regions were randomly chosen and recorded for 2-minute sessions under awake conditions. Mice received KET (10, 50, 100, 150 mg kg^{-1}) or saline (0.9%) via i.p. injection, and the same cortical regions were reimaged on average 10 minutes later based on blood vessel maps. All experiments were performed using an Olympus ×25 objective (XLPLN25XWMP2; 1.05 NA) immersed in aCSF, with ×2 digital zoom. All images were acquired at a frame rate of 2 Hz (2-μs pixel dwell time), and additional cells were imaged at both 2 Hz and 10 Hz (Supplementary Fig. 2). Image acquisition was performed using FV10-ASW version 2.0 software and analyzed post hoc using ImageJ software version 2.1.0.

Systemic and local drug delivery

Drugs delivered systemically were via a single i.p. injection: KET/Ketaset (Zoetis) at 10, 25, 35, 50, 100 and 150 mg kg^{-1} i.p.; midazolam (Hospira) at 4 mg kg^{-1}; ephedrine sulfate

(Amneal Pharmaceuticals) at 20 mg kg^{-1}; fentanyl (Novaplus) at 0.3 mg kg^{-1}; CNO (Sigma-Aldrich) at 3 mg kg^{-1} (solution of CNO in saline 0.3 mg ml^{-1}). In Extended Data Fig. 3, mice were anesthetized with 2 L min^{-1} oxygen flow mixed with inhaled concentration of sevoflurane 2% or isoflurane 1.2% (Baxter). Imaging was performed after 15 minutes of anesthesia.

Drugs of various concentrations and low injectate volumes (~1 μl) were delivered locally (KET at 50 μM and 500 μM; MK801 at 100 μM and 500 μM (M107, Sigma-Aldrich); ZD7288 at 100 μM and 500 μM (1000, Tocris); nifedipine at 100 μM (N763, Sigma-Aldrich); mecamylamine at 100 μM (M9020, Sigma-Aldrich); midazolam at 100 μM and 500 μM (Hospira); DNQX at 100 μM (D0540, Sigma-Aldrich), and, in some experiments, MK801 and ZD7288 were combined) via pressure application with a Picospritzer (20 p.s.i., 50 ms per pulse, 1 Hz, 5–10 pulses) to the surface of the S1 after removing a small bone flap (~200 μm in diameter) adjacent to the imaging window. Given the low volume of injectate, we estimate the amount of KET locally to be approximately 11 ng and 120 ng for 50 μM and 500 μM, respectively. The bone flap for drug delivery was made during head holder mounting and covered with a silicone elastomer such that it could be easily removed at the time of imaging. In some experiments, drugs were injected with Rhodamine 6G to measure the extent of spread within cortical tissue (Fig. 4 and Supplementary Fig. 3). As a control, we applied aCSF after removing the bone flap. Our choice of KET and inhibitor concentrations were similar to others performing in vivo local drug delivery[34,46-50].

Data analysis

Behavioral analysis.—Awake head-mounted mice were placed in standard housing cages, which were actively warmed by a heating blanket. Mice were assessed before and after an i.p. injection of KET or 0.9% saline. In TST (Fig. 1c), mice were suspended from the edge of a table (60 cm high) by an adhesive tape placed approximately 1 cm from the tip of the tail[24]. In TST, mice transition between complex escape movements, such as swinging and curling, mixed with smaller periods of immobility over 6 minutes of video recording. Although appearing immobile in tail suspension at 50 mg kg^{-1}, when mice are released to their cage they have normal-appearing locomotion (Extended Data Fig. 1). Videos and measurements were made using ANYMaze software (Stoelting). We also noted at 50 mg kg^{-1} and 100 mg kg^{-1}, KET elicits continuous vertical head twitching when held in TST. We defined head-twitching as rapid and sustained head shaking (duration >5 minutes) while the trunk remains stationary (Supplementary Movie).

In the marble burial test, mice are presented with 20 marbles in a large rat cage with ample bedding and assessed at 30 minutes on how many marbles were buried (2/3 of marbles must be covered by bedding) within that time. Normal mice engage with this new environment and bury marbles over this period, whereas the same mice given ketamine at 50 mg kg^{-1} or 100 mg kg^{-1} fail to bury a single marble despite movement in the cage (Extended Data Fig. 1).

For the AR assay, a circular adhesive (3M brand) measuring a diameter of 1.5 cm was placed on the snout of a head-fixed animal (Fig. 1d). The time to complete removal of the adhesive with either forelimb was measured in KET-injected and saline-injected mice. The trial timed

out at 150 seconds (considered to be a failed trial). Three trials were performed at each interval, and the average was plotted in Figs. 1, 4, 6 and 8. Trials where the adhesive fell from the snout with no forelimb movement were not counted. The AR test was performed before and after bilateral drug injections (10 minutes) to the S1 in Figs. 4, 6 and 8.

Reactivity or withdrawal of forelimb to air puff (FFW) was assessed in KET-injected and saline-injected mice (Fig. 1d). We defined a forelimb withdrawal by 5-mm movement in any direction after airpuff. If no movement was observed within 2 seconds of airpuff, this was counted as an FFW trial. We performed three trials with a 30-second break between trials. The average of three trials is presented in Fig. 1d.

EEG recordings.—Epidural EEG leads were placed in M2 and RS cortex (0.3 mm and 1.6 mm posterior to bregma, 0.65 mm lateral to bregma). EEG signals were recorded at 1,000 Hz using a 32-channel headstage (Intan Technologies) using methodology previously described[51,52]. Differential biopotentials were processed and analyzed in MATLAB (2020b, Mathworks) with the Signal Processing and Statistics and Machine Learning toolboxes and custom code to compute power spectra under saline and KET conditions using a multi-taper method (15 tapers, 10-second non-overlapping windows)[53]. Error estimation was computed using bootstrap resampling with replacement (1,000 bootstraps, across windows) to produce 95% confidence intervals. Deviations from baseline were computed by subtracting the mean baseline power spectrum from each spectral window after injection. EEG was bandpass filtered (6th order Butterworth) from 0.5 Hz to 100 Hz before spectral estimation and normalized by total power for each spectral window.

Two-photon in vivo recordings.—During recordings, motion-related artifacts were typically less than 2 μm. Vertical movements were infrequent and minimized by two metal bars attached to the animal's skull (described above) and a custom-built body support. All time-lapse images from each individual field of view were motion-corrected and referenced to a single template frame using cross-correlation image alignment (Tur-boReg plugin for ImageJ version 2.1.0). ROIs corresponding to visually identifiable somas were selected manually from the field of view shown in Extended Data Fig. 6. Imaging planes were acquired from L2/3, L4 and L5, corresponding to cells positioned 150–350 μm, 400–500 μm and more than 600 μm from the pial surface, respectively. Note that the transgenic mouse used in our study has sparse labeling throughout all layers and cortical regions[30]. As one can see in Extended Data Fig. 6, in this transgenic mouse there are approximately 5–10 neurons per L2/3 imaging region. A typical experiment would include 3–4 (randomly chosen) imaging regions per animal, yielding ~20–40 cells per animal. In Fig. 3, we included four or five L2/3 regions per mouse, yielding 25–50 cells per mouse. Because of the modest expression of GCaMP6 (as opposed to AAV-mediated expression of GCaMP6) in these transgenic mice, only 1–2 regions in L4 and L5, yielding 5–20 cells, could be obtained per mouse. This was our experience with other transgenic GCaMP mice[54,55]. Somas that could be identified in all imaging sessions were included in the dataset. Transgenic GCaMP expression was cytosolic in all imaged animals, including local drug delivery experiments. Thus, our datasets include neurons that were inactive (no transients)

during imaging sessions. Cells exhibiting nuclear expression (indicative of cytomorbidity) were extremely rare; the few such cells seen were excluded from analysis.

Analysis of KET effects on the number of calcium transients.—All the pixels inside the ROI were averaged to obtain a fluorescence trace for each ROI. Background fluorescence was calculated as the average pixel value per frame from a region without GCaMP expression (blood vessel) and subtracted from the time-series fluorescence traces. The baseline (F_0) of the fluorescence trace was estimated by the average of inactive portions of the traces (~2 seconds). We did not smooth the raw fluorescence trace (raw traces are presented without the manuscript in each figure). Three times the standard deviation (3 s.d.) of the F_0 trace was set as a threshold for detecting inactive portions in the raw fluorescence trace. The F/F_0 (%) was calculated as $F/F_0 = (F - F_0) / F_0 \times 100$. A transient was accepted as a calcium signal when its amplitude (peak value) was three times larger than the s.d. of the noise that was determined for a period of 500 ms per frame. If the calcium signal persisted or decreased but not below 3 s.d., this was counted as a single transient. If the transient descended below 3 s.d. before the rise of calcium signal, these were counted as two distinct transients (Supplementary Fig. 2b). Because of our limitation of scanning speed (2 Hz) and the long decay time constant of GCaMP6 fluorescence, it is impossible to discern actual neuronal firing rates, and, thus, our recordings likely have obscured detection of some events in both KET and saline conditions. Calcium transients were recorded over 2 minutes during wakefulness and after KET administration, and 2-minute traces are presented throughout figures. The effect of KET/saline/local drug was defined as the difference in transients in KET/saline/local drug and wakefulness. ASI is the absolute value of the difference in the number of transients recorded during wakefulness and after local or systemic KET administration. In all figures where scatter plots of calcium activity of individual neurons are shown, we compute the Pearson correlation coefficient. The P value associated with the correlation coefficient was computed by transforming the correlation coefficient to an F-statistic having n–1 and n–2 degrees of freedom, where n is the number of neurons. Negative correlation coefficients in this case mean that KET inhibits active neurons and activates silent ones.

An alternative method for showing that the effect of KET depends on the activity characteristics of a neuron during the waking state is shown in Extended Data Fig. 4. For each subset of neurons, we compute the joint distribution of the number of transients observed during wakefulness and KET. We then compared this experimentally observed joint distribution to the null hypothesis. If the probability of observing n transients during wakefulness $p_{wake}(n)$ was independent of observing k transients after KET $p_{ket}(k)$, then the joint probability of observing a neuron that fired n transients during wakefulness and k transients after KET, $p(n,k)$, should be equal to the product of the marginal probabilities, $p_{wake}(n)*p_{ket}(k)$. To compute deviations from this null hypothesis while considering the finite sample size, we used a two-sided permutation test. The indices of neurons were permuted randomly 1,000 times, and the joint distribution was computed for each bootstrap sample. Chance probability of obtaining each experimentally observed $p(n,k)$ was directly estimated from the bootstrap samples. Statistical significance of the deviation from the null hypothesis was set at $P < 0.01$.

General statistical analysis

Animals were randomly assigned to experimental groups. No statistical methods were used to pre-determine sample sizes, but our sample sizes for in vivo imaging and behavior studies are similar to those reported in our previous publications[45,54,56,57] and others[46,58,59]. The interventions were not blinded as nearly all experiments were carried out and analyzed by J.C. However, A.P., who was blinded to all experimental groups, conducted independent analyses on all datasets. Data distribution was assumed to be normal, but this was not formally tested. Mean ± s.e.m. was used to report statistics unless otherwise indicated. The statistical test used and the definition of n for each analysis are listed in the text or figure legends. Tests were computed in GraphPad Prism version 9.3.1. EEG analysis and permutation tests were performed in MATLAB (2020b) with custom scripts. Criteria for animal exclusion was pre-established: mice were excluded if the injected virus did not express. For experiments with multiple parameters and conditions, we employed Kruskal–Wallis tests for main determinants of significance. For statistically significant interaction effects within these groupings, Dunn's multiple comparisons test was used. For some behavior experiments, we used non-parametric Wilcoxon matched-pairs signed-rank test or Mann–Whitney test. Variances were similar between groups that were statistically compared. Exact P values and common levels of significance (not significant (NS) $P > 0.05$; *$P < 0.05$; **$P < 0.01$; ***$P < 0.001$) are reported in figures and legends.
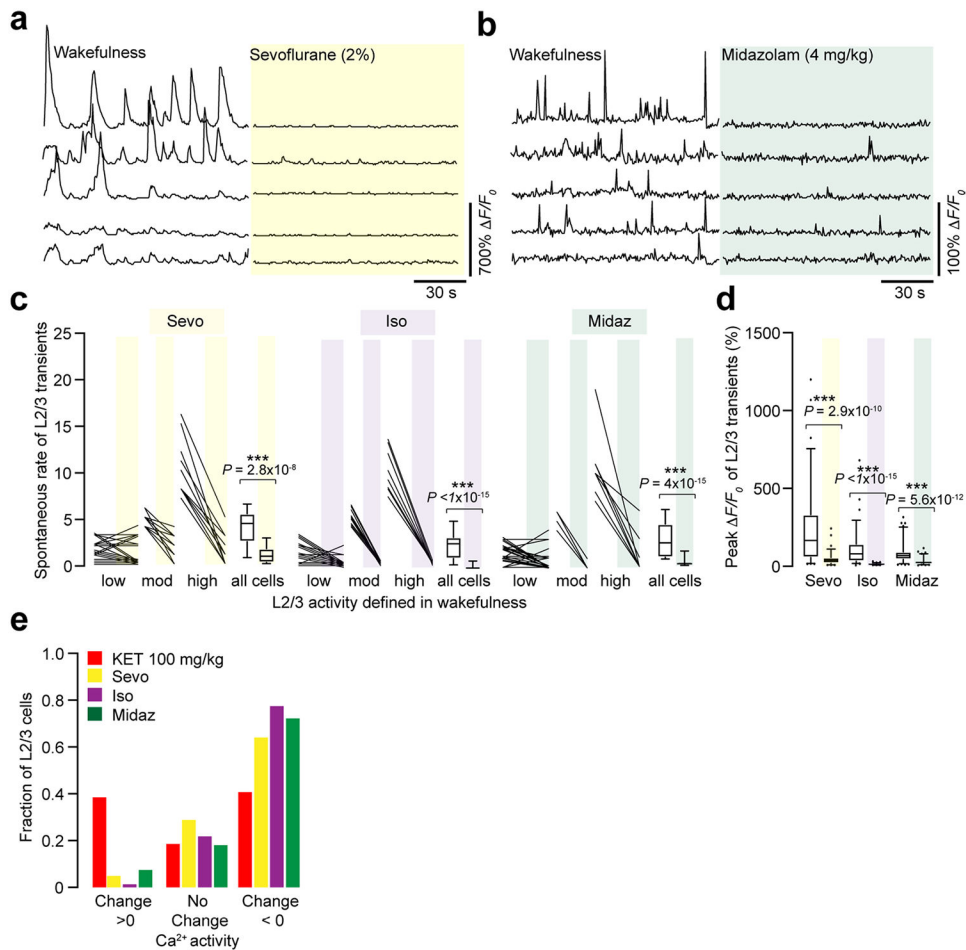
Extended Data
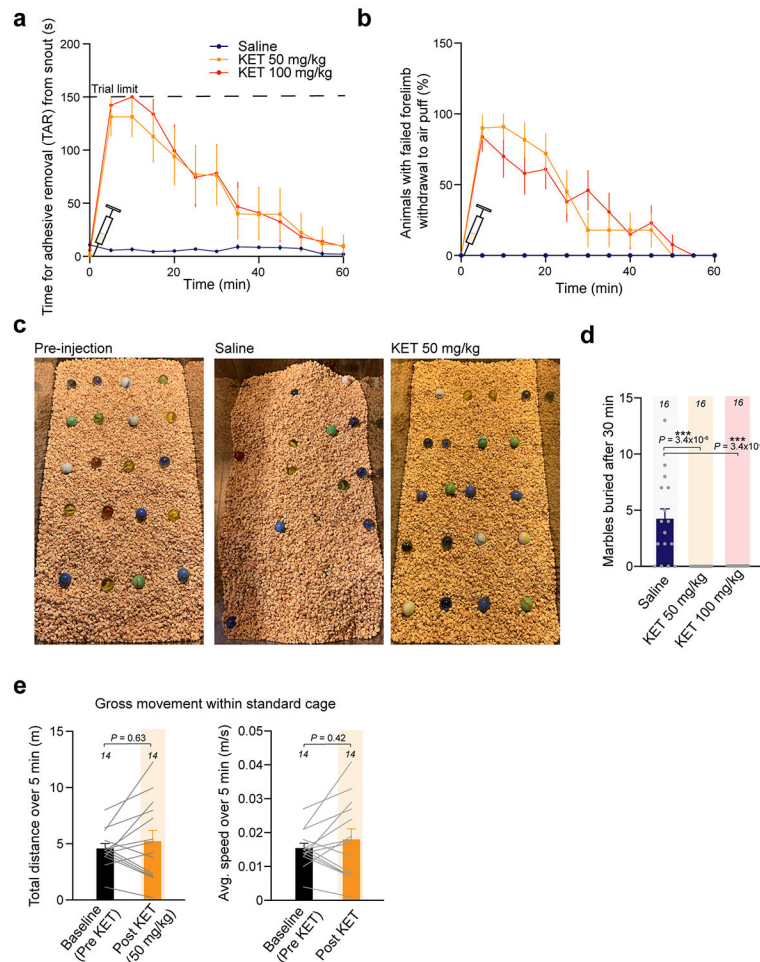
Extended Data Fig. 1 |. Subhypnotic ketamine impairs sensorimotor processing but not gross animal movement.

(**a, b**) Duration effect of single dose of ketamine (KET; 50 mg/kg: 20 mice, 100 mg/kg: 11 mice) or saline (11 mice) on time for complete removal of adhesive from snout (TAR) (**a**) and forelimb withdrawal response to air puff (**b**). (**c**) Example images of marble burial test under different conditions. Note that saline-injected mice bury a fraction of marbles over 30 min (middle image). (**d**) Summary of results of marble burial test for 16 mice in each treatment group. Mice injected with KET at either 50 or 100 mg/kg fail to bury a single marble (example image in **c**). Number of marbles buried within 30 min was 0 in KET (50 or 100 mg/kg) *vs.* 4.1 ± 1 in saline-injected mice. One-sided Kruskal-Wallis with Dunn's multiple comparisons test, *P* < 0.001. (**e**) Tracking of total distance and average speed for 14 mice over 5 min period before and after KET at 50 mg/kg in a standard mouse cage. Two-sided Wilcoxon rank test, *P* > 0.05 for both parameters. Exact *P* values in figure. Error bars show s.e.m.
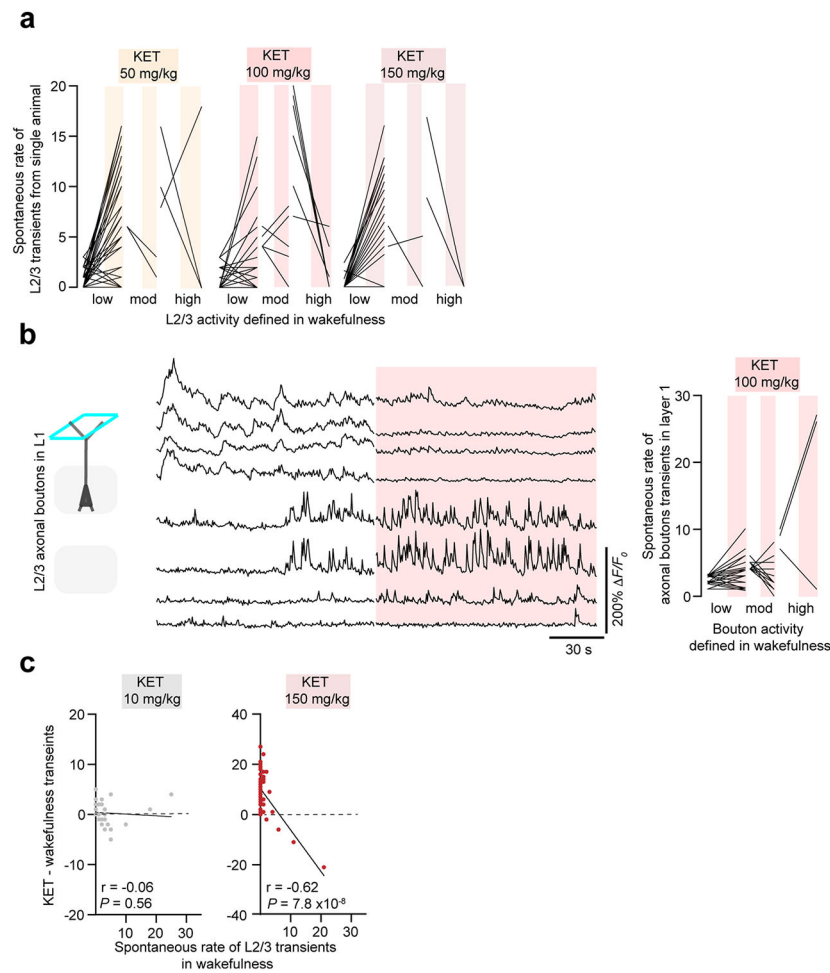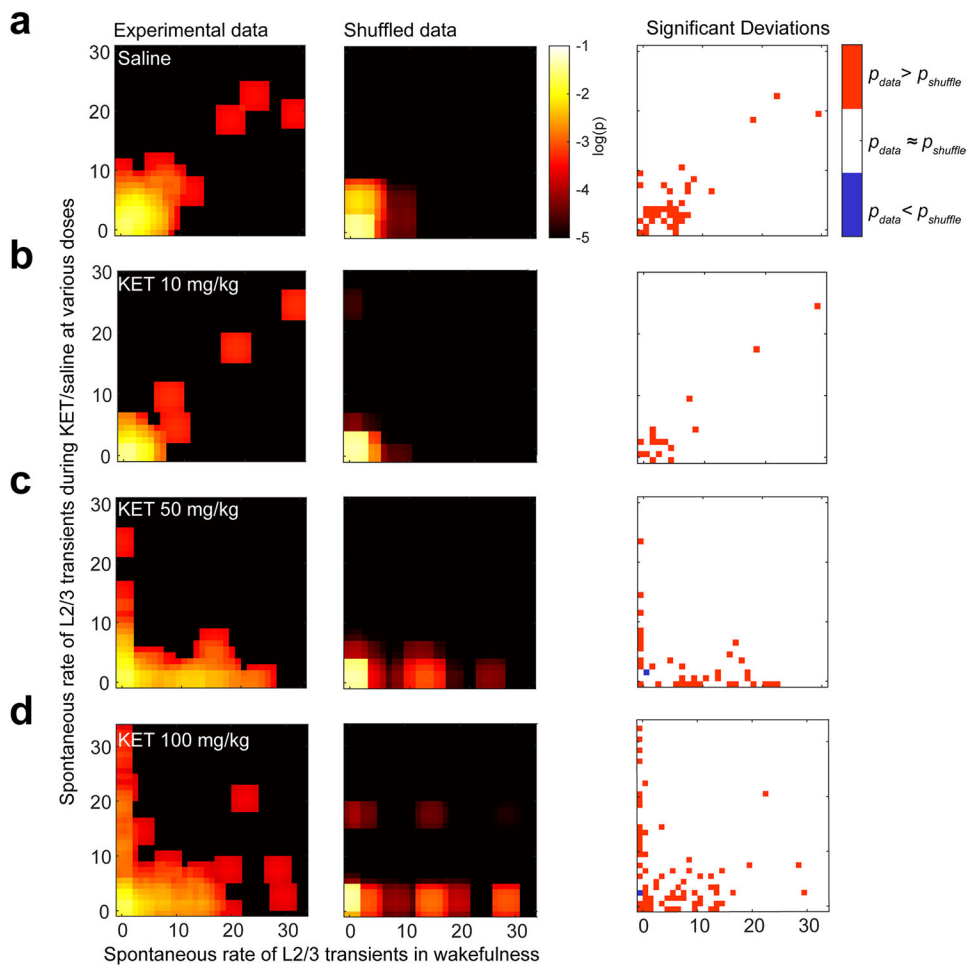
Extended Data Fig. 2 |. Various ketamine-induced layer 2/3 responses in the forelimb region of primary somatosensory cortex.

(**a**) Line scatterplots of L2/3 neurons before and after KET at different doses, 50 (49 cells from 4 regions), 100 (37 cells from 3 regions), 150 mg/kg (34 cells from 3 regions) from single animals. Scatterplot of entire L2/3 population for 50 and 100 mg/kg in Fig. 1g. (**b**) Representative fluorescent traces (left) of individual L2/3 axonal boutons imaged in layer 1 under wakefulness and KET 100 mg/kg. Line scatterplots (right) of individual boutons before and after KET 100 mg/kg reveals emergence of a switch. (**c**) Difference in calcium activity induced by KET at 10 mg/kg (left, 85 neurons from 3 mice) or 150 mg/kg IP (right, 64 neurons from 2 mice) from baseline wakefulness *vs.* wakefulness activity. KET at 150 mg/kg (one-sided Pearson correlation: r = −0.62, $P = 7.8 \times 10^{-8}$), but not at 10 mg/kg (r = −0.06, $P = 0.56$), induced a neuronal switch in L2/3 activity.

Extended Data Fig. 3 |. GABAergic hypnotic agents induce net suppression of L2/3 pyramidal cell activity.

(**a, b**) Representative GCaMP6 traces of individual L2/3 neurons under wakefulness and different hypnotic agents (**a**, sevoflurane (sevo), yellow shaded region; **b**, midazolam (midaz), green shaded region). (**c**) (Left) Line scatterplots and (Right) box plots of average spontaneous rate of L2/3 activity before and after volatile (sevo or isoflurane/iso, purple) and midaz hypnosis in S1. Spontaneous activity: Sevo group (71 neurons from 4 mice), awake: 4.0 ± 0.8 *vs.* Sevo: 1.0 ± 0.4, $P = 2.8 \times 10^{-8}$; Iso group (78 neurons from 7 mice), awake: 2.4 ± 0.5 *vs.* Iso: 0.1 ± 0.1, $P < 1 \times 10^{-15}$; Midaz group (85 neurons from 3 mice), awake: 2.8 ± 0.6 *vs.* Midaz: 0.4 ± 0.1, $P = 4 \times 10^{-15}$). (**d**) Peak F/F_0 before and after hypnosis (Sevo: awake: $238 \pm 30\%$ *vs.* Sevo: $47 \pm 5\%$, $P = 2.9 \times 10^{-10}$; Iso: awake: $102 \pm 12\%$ *vs.* Iso: $14 \pm 0.5\%$, $P < 1 \times 10^{-15}$; Midaz: awake: $83 \pm 7\%$ *vs.* Midaz: $30 \pm 2\%$, $P = 5.6 \times 10^{-12}$). Same cells from **c**. (**e**) Relative change in L2/3 activity for different hypnotic agents. Unlike KET, GABAergic hypnotics induced a uniform suppression of L2/3 neuronal activity (fraction of cells with reduced activity under GABAergic agents 65–78% *vs.* KET ~40%). While KET induced substantial activation of the network (~40–45% of cells), GABAergic agents activated fewer than 10% of cells. Box and whisker plot show min to max, centre (median), 25th and 75th percentile box bounds. One-sided Kruskal-Wallis with Dunn's multiple comparisons test in **c, d**, ***$P < 0.001$.
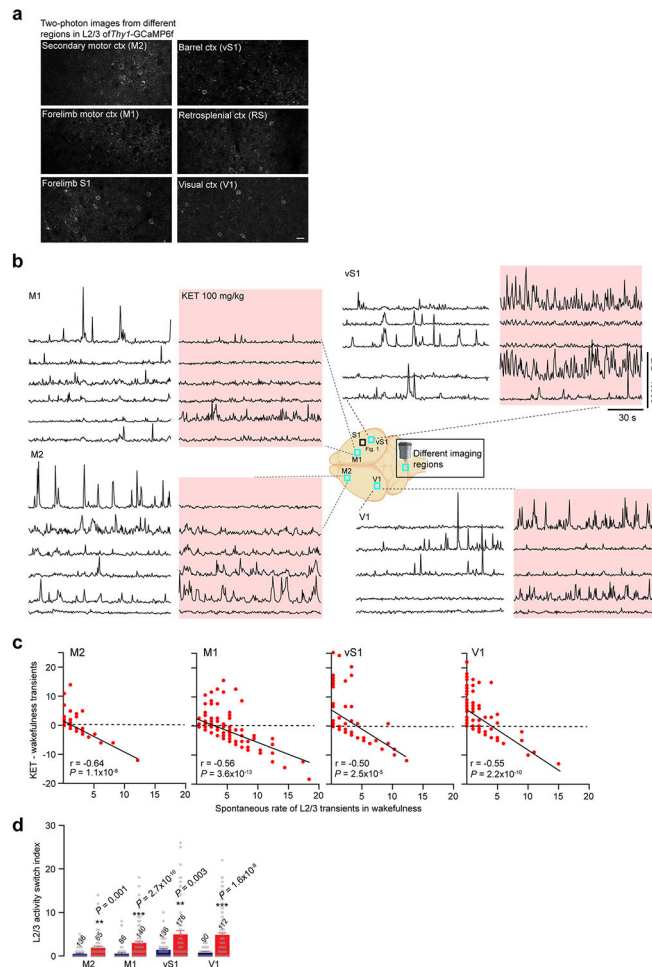
Extended Data Fig. 4 |. Ketamine-induced activity switch not explained by random changes in activity.

(a–d) Shows joint distribution of activity of L2/3 neurons under normal wakefulness (x-axis) and after ketamine (KET)/saline administration (y-axis). The left column shows the experimentally observed joint probability distribution. Middle column shows the joint distribution expected if activity after KET/saline administration did not depend on baseline activity (Methods). (a) Saline control, (b–d) KET at 10, 50, and 100 mg/kg administered systemically. The right column shows statistical deviations of the observed joint distribution (left column) from one expected if activity during normal wakefulness and after drug administration was independent (middle column). Statistical significance was computed using a two-sided permutation test consisting of shuffling neuron IDs randomly 1000 times. Deviations were statistically significant at $P < 0.01$ (bootstrap estimates). Red points indicate locations where experimentally observed probability was higher than chance, blue points indicate locations where experimentally observed probability was lower than chance, white points show areas where no statistically significant differences were detected. The regions of statistical deviations directly abutting the x and y axes under KET at 50 and 100 mg/kg indicate that KET preferentially suppresses active neurons and activates a subset of silent neurons.
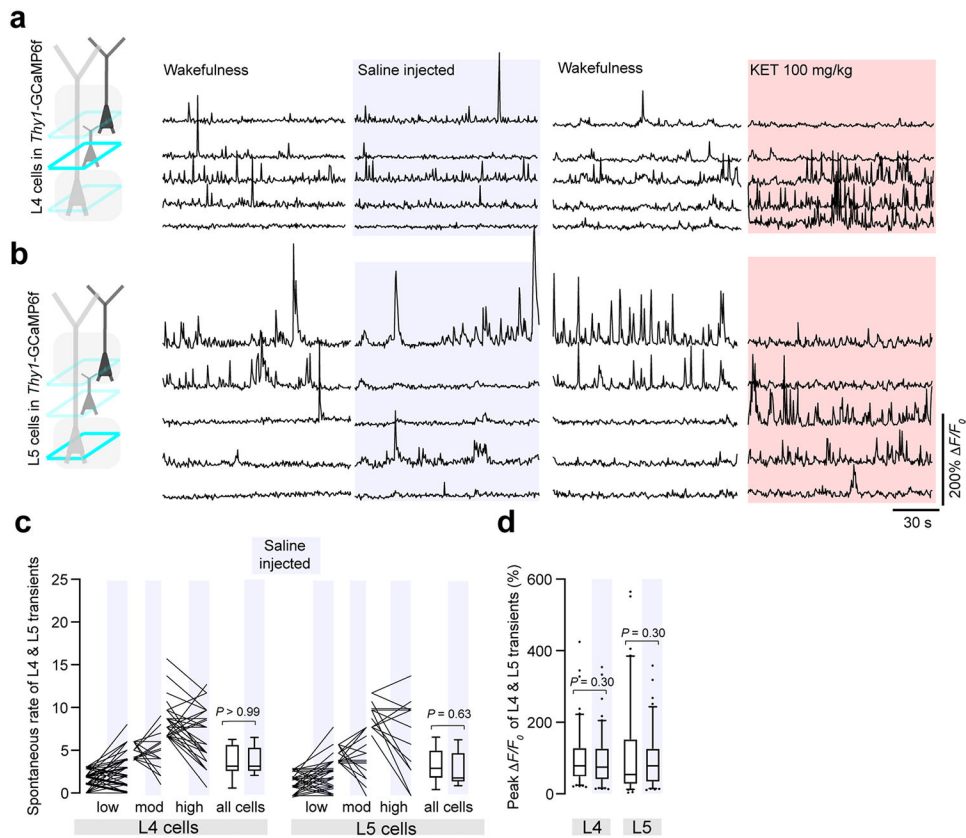
Extended Data Fig. 5 |. Layer 4 and 5 calcium responses under various conditions.
(**a, b**) Representative GCaMP6 traces of individual neurons (**a**, top for L4, **b**, bottom for L5) under wakefulness and following saline injection (left, purple shaded region) and KET at 100 mg/kg (right, red shaded region). (**c**) Line scatterplots (left) and average spontaneous activity (right) of individual L4 and L5 activity before and after saline. Saline did not significantly increase calcium activity compared to wakefulness. L4 (105 neurons from 9 mice), awake: 3.8 ± 0.6 *vs.* saline: 3.9 ± 0.5, $P > 0.99$. L5 (97 neurons from 8 mice), awake: 3.4 ± 0.7 *vs.* saline: 2.9 ± 0.7, $P = 0.63$. (**d**) Peak F/F_0 in saline-treated mice (same cells from **c**). L4, awake: $98 \pm 7\%$ *vs.* saline: $90 \pm 6\%$, $P = 0.30$. L5, awake: $112 \pm 12\%$ *vs.* saline: $95 \pm 7\%$, $P = 0.30$. Box and whisker plot show min to max, centre (median), 25th and 75th percentile box bounds. One-sided Kruskal-Wallis with Dunn's multiple comparisons test in **c, d**.

Extended Data Fig. 6 |. Ketamine at 100 mg/kg induces a neuronal switch in L2/3 activity across the neocortex.

(**a**) Two-photon images of L2/3 neurons from various cortical regions in *Thy1*-GCaMP6f mice. Scale bar: 20 μm. (**b**) Cartoon of mouse brain in center of panel demarcates imaging locations (teal boxes) across the neocortex. Surrounding traces are representative L2/3 neurons from these regions under wakefulness and KET 100 mg/kg. (**c**) The effect of KET was negatively correlated with the activity in wakefulness across all imaged cortical regions. M2 (65 from 4 mice; r = −0.64, $P = 1.1 \times 10^{-8}$), M1 (140 from 4 mice; r = −0.56, $P = 3.6 \times 10^{-13}$), vibrissal (v) S1 (65 from 2 mice; r = −0.50, $P = 2.5 \times 10^{-5}$), and V1 (120 from 4 mice; r = −0.55, $P = 2.2 \times 10^{-10}$). (**d**) L2/3 activity switch index across saline and KET-injected mice for various regions. M2 ($P = 0.001$), M1 ($P = 2.7 \times 10^{-10}$), vS1 ($P = 0.003$), and V1 ($P = 1.6 \times 10^{-8}$). Error bars show s.e.m. One-sided Pearson correlations in **c**, One-sided Kruskal-Wallis with Dunn's multiple comparisons test in **d**, ***$P < 0.001$.
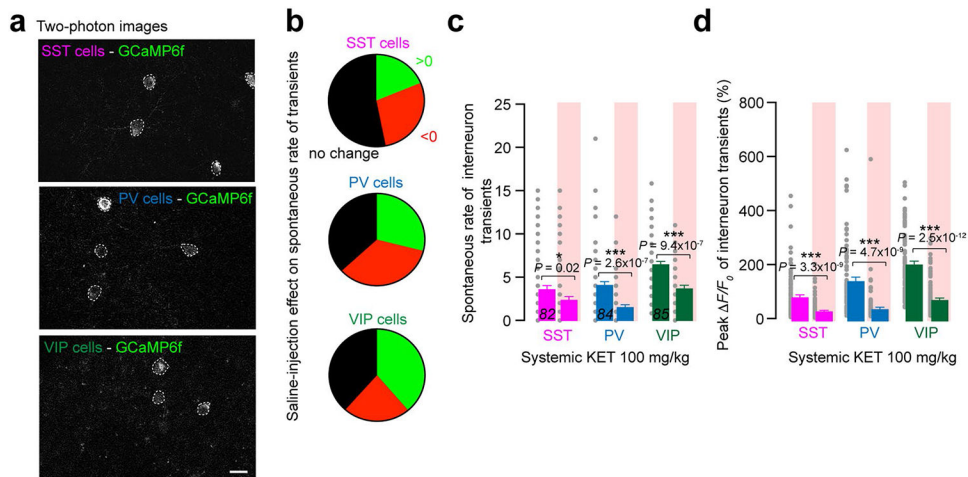
Extended Data Fig. 7 |. Labelling different inhibitory interneurons subtypes in the somatosensory cortex with GCaMP6 and their responses to ketamine at 100 mg/kg.
(**a**) Example two-photon imaging fields of interneuron subtypes (SST, pink; PV cells, blue; VIP cells, green) expressing GCaMP6f in the S1. Interneurons outlined with white circles. Scale bar: 20 μm. Representative images carried out on at least 3 animals per group. (**b**) Pie graphs show the portion of cells increasing (green)/decreasing (red)/no change (black) following saline administration for each interneuron subtypes. (**c, d**) Comparison between spontaneous rate of activity (**c**) and peak signals (**d**) across interneuron subtypes following KET at 100 mg/kg. SST: 82 cells from 6 mice, PV: 84 cells from 4 mice, VIP: 85 mice from 5 mice (cell numbers per subtype italicized in **c**). Note the strong reduction of spontaneous interneuron activity and peak signals (Onesided Kruskal-Wallis with Dunn's multiple comparisons for **c**: $P < 0.05$ for SST and $P < 0.001$ for all other comparisons; **d**: $P < 0.001$ for all comparisons). Exact P values in figure. Error bars show s.e.m.
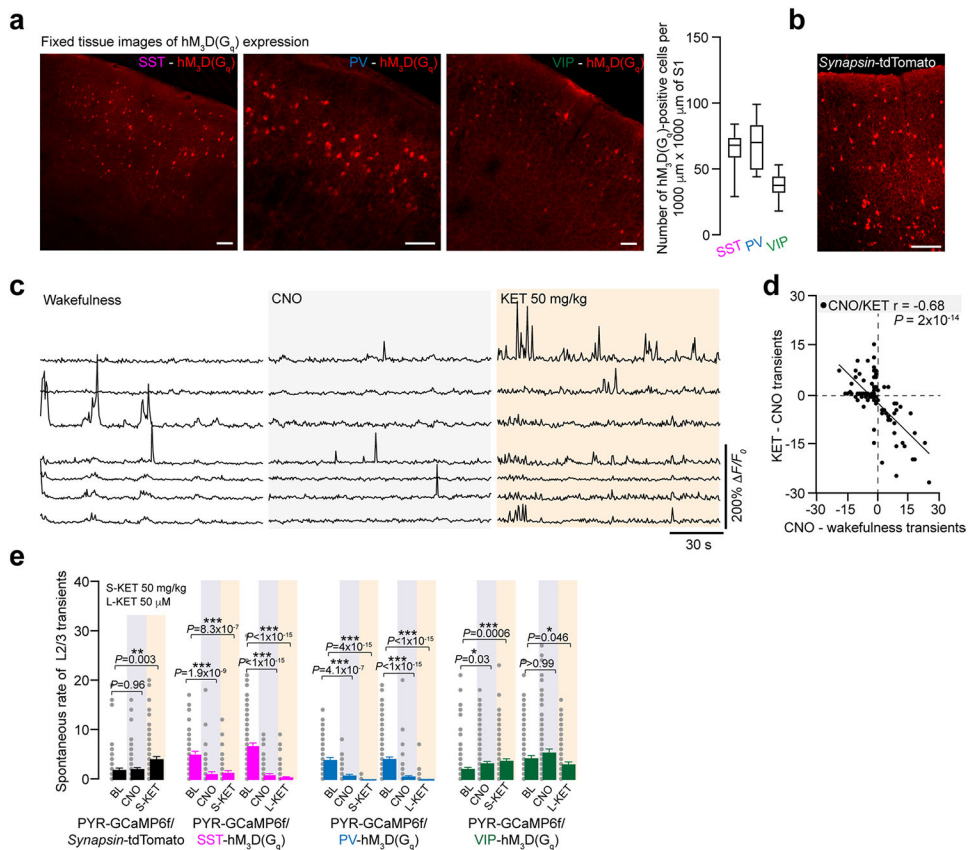
Extended Data Fig. 8 |. Systemic administration of CNO does not impair ketamine's neuronal activity switch in L2/3 neurons of S1.

(**a**) Coronal slices (left) of S1 region from interneuron-specific Cre-positive mice expressing DREADD variant $hM_3D(G_q)$-mCherry. Scale bar: 100 μm. (Right) Number of $hM_3D(G_q)$-mCherry positive cells in a 1 mm^2 region of forelimb S1 (slice thickness 30 μm). 15 (SST), 16 (PV), and 16 (VIP) S1 slices from 4 mice in each group. Box and whisker plot show min to max, centre (median), 25th and 75th percentile box bounds. (**b**) Coronal slice of S1 region from mouse expressing AAV-*hSynapsin-1*-tdTomato. Scale bar: 100 μm. (**c**) Representative traces of L2/3 pyramidal cells under wakefulness, CNO, then KET at 50 mg/kg in mice expressing AAV-*hSynapsin-1*-tdTomato. (**d**) L2/3 cell activity in the setting of CNO *vs.* its response to KET at 50 mg/kg in mice expressing AAV-hSyn1-tdTomato (97 neurons from 3 mice). KET at 50 mg/kg induced a strong neuronal switch (Pearson correlation r $= -0.68$, $P = 2 \times 10^{-14}$) and a significant elevation in activity switch index (KET 4.9 ± 0.5) whereas CNO injection did not (1.8 ± 0.2, $P > 0.05$). (**e**) Spontaneous rate of activity of L2/3 pyramidal neurons before/baseline (BL), after interneuron subtype activation (CNO activation of $hM_3D(G_q)$) and following KET treatment at 50 mg/kg. Same cells from Fig. 6d. One-sided Kruskal-Wallis, $P < 0.001$ with Dunn's multiple comparisons and P values listed in graph. Representative images and traces carried out on at least 3 animals per group. Error bars show s.e.m. *$P < 0.05$, **$P < 0.01$, ***$P < 0.001$.
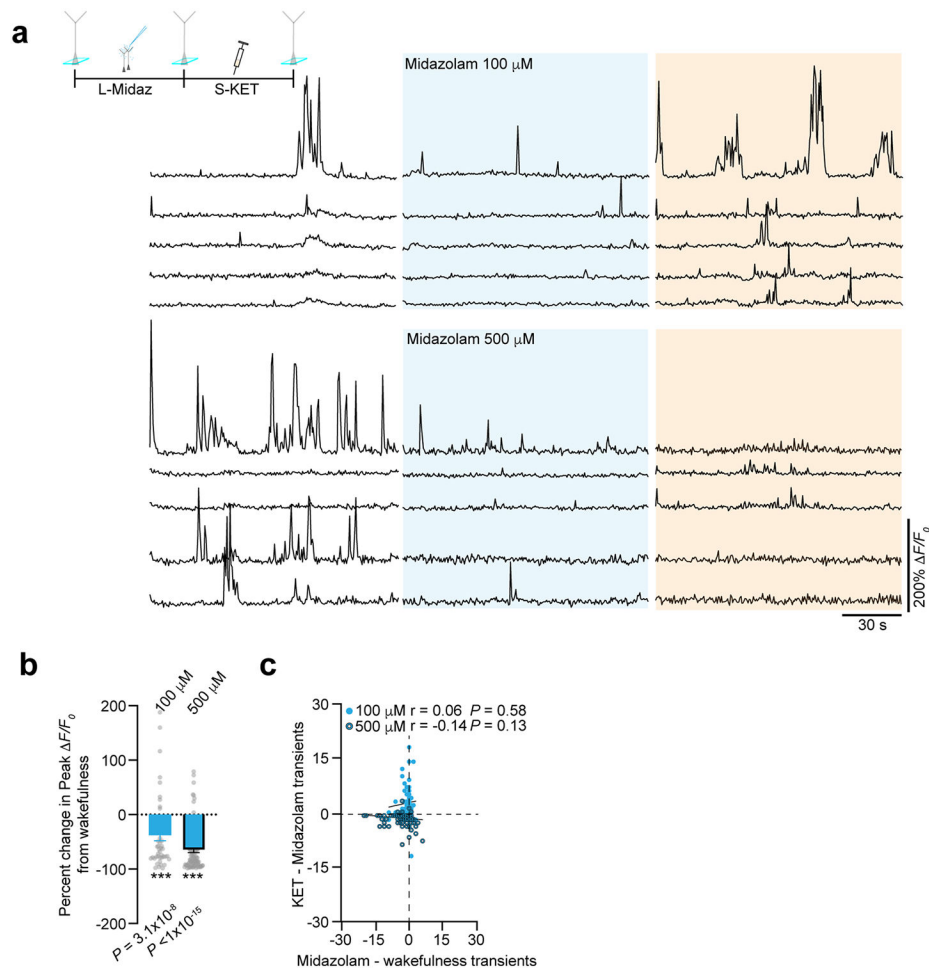
Extended Data Fig. 9 |. Ketamine-induced neuronal switch attenuated in the presence of local midazolam to S1.
(**a**) Representative GCaMP6 traces of L2/3 pyramidal neurons under wakefulness and local (L-) midazolam at 100 (79 neurons from 3 mice) and 500 (125 neurons from 3 mice) μM. (**b**) L-midazolam reduced the normalized calcium response as compared to wakefulness indicating the likely facilitation of spontaneous $GABA_A$ receptor activity. Same cells from **a**. Error bars show s.e.m. (**c**) Scatterplot of L2/3 activity in the presence of L-midazolam vs. KET at 50 mg/kg. KET-induced neuronal switch was attenuated in the presence of L-midazolam (100 μM: r = 0.06, $P = 0.58$; 500 μM: r = −0.14, $P = 0.13$). Two-sided Wilcoxon matched-pairs signed-rank test in **b**, Pearson correlations in **c**. ***$P < 0.001$.
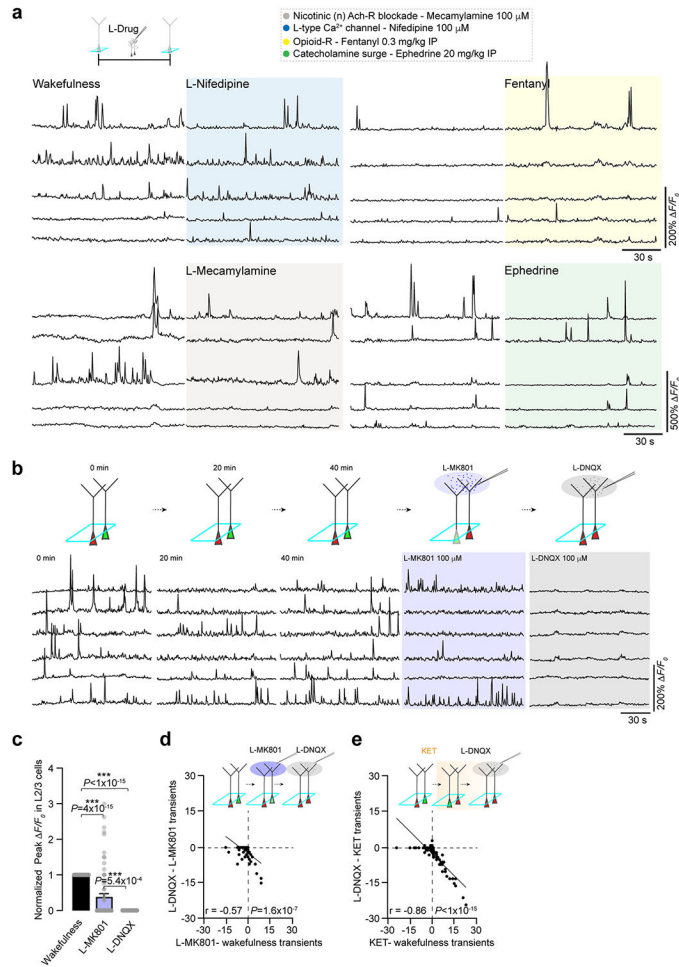
Extended Data Fig. 10 |. Layer 2/3 calcium responses under various drug conditions.
(**a**) Representative GCaMP6 traces of individual L2/3 neurons from S1 under wakefulness
and following local (nifedipine at 100 μM and mecamylamine at 100 μM) or systemic
(fentanyl at 0.3 mg/kg IP and ephedrine at 20 mg/kg IP) drug injection (color shaded
regions). These potential KET molecular targets were ineffective inducers of an activity
switch in L2/3 neurons (see Fig. 7). (**b**) Experimental design (top) for sequential local (L-)
blockade of NMDA-R and AMPA-R *in vivo*. (Bottom) Representative GCaMP6 traces of
L2/3 pyramidal neurons under wakefulness followed over 40 min followed by sequential
delivery of L-MK801 at 100 μM and then DNQX at 100 μM (73 cells from 2 mice). (**c**)
Compared to baseline recording in wakefulness, L-MK801 significantly reduced (61%) the
L2/3 activity. The remaining cohort of active cells in the presence of L-MK801 could be
completely silenced in the presence of L-DNQX. Same cells from **b**. One-sided Kruskal-
Wallis with Dunn's multiple comparisons test in **c**. (**d, e**) Scatter plots of L2/3 activity
modulated by either L-MK801 (73 neurons from 2 mice, one-sided Pearson correlation r =
−0.57, $P = 1.6 \times 10^{-7}$) or systemic KET at 50 mg/kg (94 neurons from 3 mice, $r = −0.86$, $P
= < 1 \times 10^{-15}$) *vs.* L-DNQX effect. L-DNQX blocks newly activated cells induced by KET.
Error bars show s.e.m. ***$P < 0.001$.

Supplementary Material

Refer to Web version on PubMed Central for supplementary material.

Acknowledgements

Data availability

Figures and associated data will be available to the scientific community via figshare.

References

1. Sleigh J, Harvey M, Voss L & Denny B Ketamine—more mechanisms of action than just NMDA blockade. Trends Anaesth. Crit. Care 4, 76–81 (2014).

2. Berman RM et al. Antidepressant effects of ketamine in depressed patients. Biol. Psychiatry 47, 351–354 (2000). [PubMed: 10686270]

3. Krystal JH et al. Subanesthetic effects of the noncompetitive NMDA antagonist, ketamine, in humans. Psychotomimetic, perceptual, cognitive, and neuroendocrine responses. Arch. Gen. Psychiatry 51, 199–214 (1994). [PubMed: 8122957]

4. Li D & Mashour GA Cortical dynamics during psychedelic and anesthetized states induced by ketamine. Neuroimage 196, 32–40 (2019). [PubMed: 30959192]

5. Akeju O. et al. Electroencephalogram signatures of ketamine anesthesia-induced unconsciousness. Clin. Neurophysiol 127, 2414–2422 (2016). [PubMed: 27178861]

6. Schwartz MS, Virden S & Scott DF Effects of ketamine on the electroencephalograph. Anaesthesia 29, 135–140 (1974). [PubMed: 4819066]

7. Corssen G & Domino EF Dissociative anesthesia: further pharmacologic studies and first clinical experience with the phencyclidine derivative CI-581. Anesth. Analg 45, 29–40 (1966). [PubMed: 5325977]

8. Domino EF Taming the ketamine tiger. 1965. Anesthesiology 113, 678–684 (2010). [PubMed: 20693870]

9. Domino EF, Chodoff P & Corssen G Pharmacologic effects of Ci-581, a new dissociative anesthetic, in man. Clin. Pharmacol. Ther 6, 279–291 (1965). [PubMed: 14296024]

10. Vesuna S. et al. Deep posteromedial cortical rhythm in dissociation. Nature 586, 87–94 (2020). [PubMed: 32939091]

11. Abdallah CG et al. The effects of ketamine on prefrontal glutamate neurotransmission in healthy and depressed subjects. Neuropsychopharmacology 43, 2154–2160 (2018). [PubMed: 29977074]

12. Moghaddam B, Adams B, Verma A & Daly D Activation of glutamatergic neurotransmission by ketamine: a novel step in the pathway from NMDA receptor blockade to dopaminergic and cognitive disruptions associated with the prefrontal cortex. J. Neurosci 17, 2921–2927 (1997). [PubMed: 9092613]

13. Ali F. et al. Ketamine disinhibits dendrites and enhances calcium signals in prefrontal dendritic spines. Nat. Commun 11, 72 (2020). [PubMed: 31911591]

14. Homayoun H & Moghaddam B NMDA receptor hypofunction produces opposite effects on prefrontal cortex interneurons and pyramidal neurons. J. Neurosci 27, 11496–11500 (2007). [PubMed: 17959792]

15. Patel IM & Chapin JK Ketamine effects on somatosensory cortical single neurons and on behavior in rats. Anesth. Analg 70, 635–644 (1990). [PubMed: 2344058]

16. Moda-Sava RN et al. Sustained rescue of prefrontal circuit dysfunction by antidepressant-induced spine formation. Science 364, eaat8078 (2019). [PubMed: 30975859]

17. Ng LHL et al. Ketamine and selective activation of parvalbumin interneurons inhibit stress-induced dendritic spine elimination. Transl. Psychiatry 8, 272 (2018). [PubMed: 30531859]

18. MacDonald JF, Miljkovic Z & Pennefather P Use-dependent block of excitatory amino acid currents in cultured neurons by ketamine. J. Neurophysiol 58, 251–266 (1987). [PubMed: 2443623]

19. Chen X, Shu S & Bayliss DA HCN1 channel subunits are a molecular substrate for hypnotic actions of ketamine. J. Neurosci 29, 600–609 (2009). [PubMed: 19158287]

20. Gerhard DM et al. GABA interneurons are the cellular trigger for ketamine's rapid antidepressant actions. J. Clin. Invest 130, 1336–1349 (2020). [PubMed: 31743111]

21. Freund TF & Katona I Perisomatic inhibition. Neuron 56, 33–42 (2007). [PubMed: 17920013]

22. Chiu CQ et al. Compartmentalization of GABAergic inhibition by dendritic spines. Science 340, 759–762 (2013). [PubMed: 23661763]

23. Pi H-J et al. Cortical interneurons that specialize in disinhibitory control. Nature 503, 521–524 (2013). [PubMed: 24097352]

24. Cryan JF, Mombereau C & Vassout A The tail suspension test as a model for assessing antidepressant activity: review of pharmacological and genetic studies in mice. Neurosci. Biobehav. Rev 29, 571–625 (2005). [PubMed: 15890404]

25. Corne SJ & Pickering RW A possible correlation between drug-induced hallucinations in man and a behavioural response in mice. Psychopharmacologia 11, 65–78 (1967). [PubMed: 5302272]

26. Broekkamp CL, Rijk HW, Joly-Gelouin D & Lloyd KL Major tranquillizers can be distinguished from minor tranquillizers on the basis of effects on marble burying and swim-induced grooming in mice. Eur. J. Pharmacol 126, 223–229 (1986). [PubMed: 2875886]

27. Bouet V. et al. The adhesive removal test: a sensitive method to assess sensorimotor deficits in mice. Nat. Protoc 4, 1560–1564 (2009). [PubMed: 19798088]

28. Blain-Moraes S, Lee U, Ku S, Noh G & Mashour GA Electroencephalographic effects of ketamine on power, cross-frequency coupling, and connectivity in the alpha bandwidth. Front. Syst. Neurosci 8, 114 (2014). [PubMed: 25071473]

29. Sachidhanandam S, Sreenivasan V, Kyriakatos A, Kremer Y & Petersen CCH Membrane potential correlates of sensory perception in mouse barrel cortex. Nat. Neurosci 16, 1671–1677 (2013). [PubMed: 24097038]

30. Dana H. et al. *Thy1*-GCaMP6 transgenic mice for neuronal population imaging in vivo. PLoS ONE 9, e108697 (2014). [PubMed: 25250714]

31. Lu J. et al. Role of endogenous sleep-wake and analgesic systems in anesthesia. J. Comp. Neurol 508, 648–662 (2008). [PubMed: 18383504]

32. Nelson CL, Burk JA, Bruno JP & Sarter M Effects of acute and repeated systemic administration of ketamine on prefrontal acetylcholine release and sustained attention. Psychopharmacology (Berl.) 161, 168–179 (2002). [PubMed: 11981597]

33. Långsjö JW et al. S-ketamine anesthesia increases cerebral blood flow in excess of the metabolic needs in humans. Anesthesiology 103, 258–268 (2005). [PubMed: 16052107]

34. Ouelhazi A. et al. Effects of ketamine on orientation selectivity and variability of neuronal responses in primary visual cortex. Brain Res. 1725, 146462 (2019). [PubMed: 31539548]

35. Quirk MC, Sosulski DL, Feierstein CE, Uchida N & Mainen ZF A defined network of fast-spiking interneurons in orbitofrontal cortex: responses to behavioral contingencies and ketamine administration. Front. Syst. Neurosci 3, 13 (2009). [PubMed: 20057934]

36. Urban DJ & Roth BL DREADDs (designer receptors exclusively activated by designer drugs): chemogenetic tools with therapeutic utility. Annu. Rev. Pharmacol. Toxicol 55, 399–417 (2015). [PubMed: 25292433]

37. Miller RD et al. Miller's Anesthesia (Elsevier Health Sciences, 2014).

38. Mashour GA Top-down mechanisms of anesthetic-induced unconsciousness. Front. Syst. Neurosci 8, 115 (2014). [PubMed: 25002838]

39. Constantinidis C & Goldman-Rakic PS Correlated discharges among putative pyramidal neurons and interneurons in the primate prefrontal cortex. J. Neurophysiol 88, 3487–3497 (2002). [PubMed: 12466463]

40. Rao SG, Williams GV & Goldman-Rakic PS Isodirectional tuning of adjacent interneurons and pyramidal cells during working memory: evidence for microcolumnar organization in PFC. J. Neurophysiol 81, 1903–1916 (1999). [PubMed: 10200225]

41. Alexander L. et al. Fractionating blunted reward processing characteristic of anhedonia by over-activating primate subgenual anterior cingulate cortex. Neuron 101, 307–320 (2019). [PubMed: 30528065]

42. Zhou H. et al. Ketamine reduces aversion in rodent pain models by suppressing hyperactivity of the anterior cingulate cortex. Nat. Commun 9, 3751 (2018). [PubMed: 30218052]

43. Tokay T. et al. HCN1 channels constrain DHPG-induced LTD at hippocampal Schaffer collateral-CA1 synapses. Learn. Mem 16, 769–776 (2009). [PubMed: 19940037]

44. Zhang K. Essential roles of AMPA receptor GluA1 phosphorylation and presynaptic HCN channels in fast-acting antidepressant responses of ketamine. Sci. Signal 9, ra123 (2016). [PubMed: 27965425]

45. Cichon J & Gan W-B Branch-specific dendritic Ca^{2+} spikes cause persistent synaptic plasticity. Nature 520, 180–185 (2015). [PubMed: 25822789]

46. Li W, Ma L, Yang G & Gan W-B REM sleep selectively prunes and maintains new synapses in development and learning. Nat. Neurosci 20, 427–437 (2017). [PubMed: 28092659]

47. Zhou Y. REM sleep promotes experience-dependent dendritic spine elimination in the mouse cortex. Nat. Commun 11, 4819 (2020). [PubMed: 32968048]

48. Suzuki M & Larkum ME Dendritic calcium spikes are clearly detectable at the cortical surface. Nat. Commun 8, 276 (2017). [PubMed: 28819259]

49. David F. et al. Suppression of hyperpolarization-activated cyclic nucleotide-gated channel function in thalamocortical neurons prevents genetically determined and pharmacologically induced absence seizures. J. Neurosci 38, 6615–6627 (2018). [PubMed: 29925625]

50. Labarrera C. Adrenergic modulation regulates the dendritic excitability of layer 5 pyramidal neurons in vivo. Cell Rep. 23, 1034–1044 (2018). [PubMed: 29694883]

51. Wasilczuk AZ, Proekt A, Kelz MB & McKinstry-Wu AR High-density electroencephalographic acquisition in a rodent model using low-cost and open-source resources. J. Vis. Exp 117, 54908 (2016).

52. Siegle JH Open Ephys: an open-source, plugin-based platform for multichannel electrophysiology. J. Neural Eng 14, 045003 (2017). [PubMed: 28169219]

53. Hudson AE, Calderon DP, Pfaff DW & Proekt A Recovery of consciousness is mediated by a network of discrete metastable activity states. Proc. Natl Acad. Sci. USA 111, 9283–9288 (2014). [PubMed: 24927558]

54. Cichon J. et al. Imaging neuronal activity in the central and peripheral nervous systems using new *Thy1.2*-GCaMP6 transgenic mouse lines. J. Neurosci. Methods 334, 108535 (2020). [PubMed: 31972184]

55. Chen Q. et al. Imaging neural activity using *Thy1*-GCaMP transgenic mice. Neuron 76, 297–308 (2012). [PubMed: 23083733]

56. Cichon J, Blanck TJJ, Gan W-B & Yang G Activation of cortical somatostatin interneurons prevents the development of neuropathic pain. Nat. Neurosci 20, 1122–1132 (2017). [PubMed: 28671692]

57. Yang G. et al. Sleep promotes branch-specific formation of dendritic spines after learning. Science 344, 1173–1178 (2014). [PubMed: 24904169]

58. Adler A, Zhao R, Shin ME, Yasuda R & Gan W-B Somatostatin-expressing interneurons enable and maintain learning-dependent sequential activation of pyramidal neurons. Neuron 102, 202–216 (2019). [PubMed: 30792151]

59. Zhao R. et al. Neuropathic pain causes pyramidal neuronal hyperactivity in the anterior cingulate cortex. Front. Cell. Neurosci 12, 107 (2018). [PubMed: 29731710]
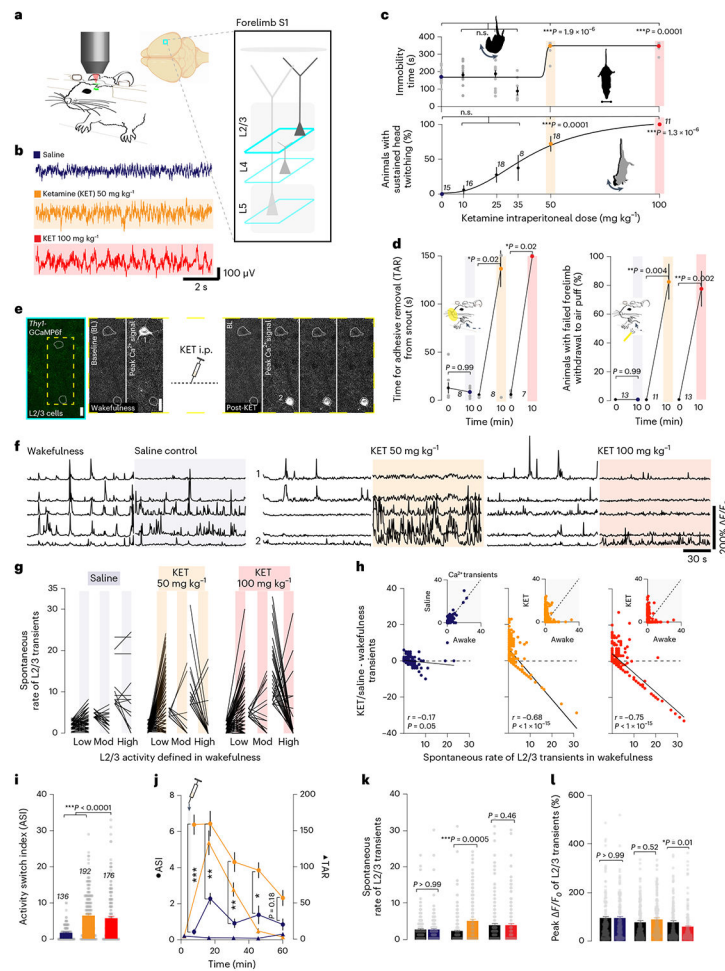
Fig. 1 |. KET induces a switch in the active population of L2/3 neurons in S1.

a, Cartoon of head-restrained animal under two-photon microscope (left) and imaging locations at various depths (teal boxes) across cortical column (right) of the forelimb region of S1 cortex. **b**, EEG traces under wakefulness (saline, purple) and KET at 50 mg kg^{-1} (orange) and 100 mg kg^{-1} (red). **c**, Top: Mice held in tail suspension (TS) exhibit escape-like behaviors and spend less time immobile. KET at 50 mg kg^{-1} and 100 mg kg^{-1} (average immobility time was $349 \pm 7/348 \pm 7$ seconds (50/100 mg kg^{-1}) versus 172 ± 10 seconds in wakefulness) eliminates escape-like movements, with immobility time approaching maximum (360 seconds, dashed line), Kruskal–Wallis: *P* values for KET 10, 25, 35 mg kg^{-1}: >0.99, >0.99 and 0.65 versus KET 50 mg kg^{-1} and 100 mg kg^{-1}: $P = 1.9 \times 10^{-6}$ and $P = 0.0001$. Bottom: In mice in TS, KET induces a dose-dependent sustained head-twitching response with no truncal movements (72 ± 11 / 100% of animals in KET (50/100 mg kg^{-1}) versus 0% in saline controls), Kruskal–Wallis: *P* values for KET 10, 25 and 35 mg kg^{-1}: >0.99, 0.52 and 0.40 versus KET 50 mg kg^{-1} and 100 mg kg^{-1}: $P = 0.0001$ and $P = 1.3 \times 10^{-6}$. **d**, Sensorimotor function was assessed by measuring the time for complete removal of adhesive tape (TAR) from snout (left) and forelimb withdrawal to air puff (right). KET induced significant impairments in sensory responsiveness at 50 mg kg^{-1} and 100 mg kg^{-1}. TAR: average at 10 minutes after injection was 131 ± 19 and 150

± 0 seconds after KET 50 mg kg^{-1} and 100 mg kg^{-1} versus 7 ± 2 seconds in controls, Wilcoxon rank test: $P = 0.02$ and $P = 0.02$ for KET 50 mg kg^{-1} and 100 mg kg^{-1}. FFW: average at 10 minutes after injection was 82% ± 12% and 77% ± 12% after KET 50 mg kg^{-1} and 100 mg kg^{-1} versus 0.1% ± 0.1% in controls, $P < 0.01$, Wilcoxon rank test: $P = 0.004$ and $P = 0.002$ for KET 50 mg kg^{-1} and 100 mg kg^{-1}. **e**, Two-photon image of L2/3 cortical region (teal box) in S1 from *Thy1*-GCaMP6f mouse. Note the sparse labeling of GCaMP in transgenic line. Cropped region (yellow dashed box) shows two pyramidal neurons outlined with white dashed circles. Active cell inactivates after KET administration (cell 1). A previously inactive cell activates after KET administration (cell 2). Multiple peak F/F_0 images (3) during KET state are shown. Scale bar, 20 μm. **f**, Representative GCaMP6 traces of individual neurons under wakefulness/saline and wakefulness/KET. Cells 1 and 2 from KET 50 mg kg^{-1}. **g**, Line scatter plots of individual L2/3 cells show activity changes before and after saline ($n = 136$ neurons from seven mice), KET at 50 mg kg^{-1} ($n = 192$ neurons from eight mice) and 100 mg kg^{-1} ($n = 176$ neurons from nine mice). Low/moderate/high bins defined in wakefulness. Individual animal KET-induced switching in Extended Data Fig. 2a. **h**, Difference in calcium transients induced by KET or saline from baseline wakefulness versus wakefulness activity in all L2/3 cells recorded. Note the strong negative correlation between activity in wakefulness and KET at 50 mg kg^{-1} (Pearson correlation: $r = -0.68$, $P < 1 \times 10^{-15}$) and 100 mg kg^{-1} ($r = -0.75$, $P < 1 \times 10^{-15}$) versus saline ($r = -0.17$, $P = 0.05$). Subplot in upper right shows the number of transients in the wakefulness versus saline/KET. **i**, KET significantly increases the L2/3 ASI as compared to saline-injected mice (KET 50 mg kg^{-1}: 6.4 ± 0.4; KET 100 mg kg^{-1}: 5.7 ± 0.5 versus saline: 1.7 ± 0.2), Kruskal–Wallis: $P < 0.001$ followed by Dunn's multiple comparison test, $P = 1.0 \times 10^{-15}$ and 7.2×10^{-9} for KET 50 mg kg^{-1} and 100 mg kg^{-1}. **j**, Tracking ASI (circles) and TAR (triangles) over 1 hour after KET injection ($n = 78$ cells from nine regions of three mice) or saline injection ($n = 48$ cells from five regions of three mice) (multiple unpaired *t*-tests for ASI, $P = 2 \times 10^{-5}$ for 5 minutes ($t_{12} = 7.94$), $P = 0.005$ and $P = 0.003$ for 15 minutes and 30 minutes ($t_{12} = 4.32$ and $t_{12} = 4.54$), $P = 0.02$ for 45 minutes ($t_{12} = 3.65$), $P = 0.18$ for 60 minutes ($t_{12} = 2.36$)). Note the ASI and TAR trend together in the KET-treated group. **k,l**, Average spontaneous rate of calcium transients over 2-minute recordings (Kruskal–Wallis: $P = 0.0014$ followed by Dunn's multiple comparisons test, $P = 0.0005$ for KET 50 mg kg^{-1}) and peak F/F_0 (Kruskal–Wallis: $P < 0.0001$ followed by Dunn's multiple comparisons test, $P = 0.01$ for KET 100 mg kg^{-1}) in L2/3 under KET and saline conditions. Comparisons made to baseline, pre-injection recording. *n* for animals in **c,d** and same cells italicized in **i** used in **g,h** and **k,l**, Representative images and traces carried out on at least three animals per group. Kruskal–Wallis one-sided, Wilcoxon rank two-sided and Pearson correlation one-sided. Error bars show s.e.m. *$P < 0.05$, **$P < 0.01$ and ***$P < 0.001$.
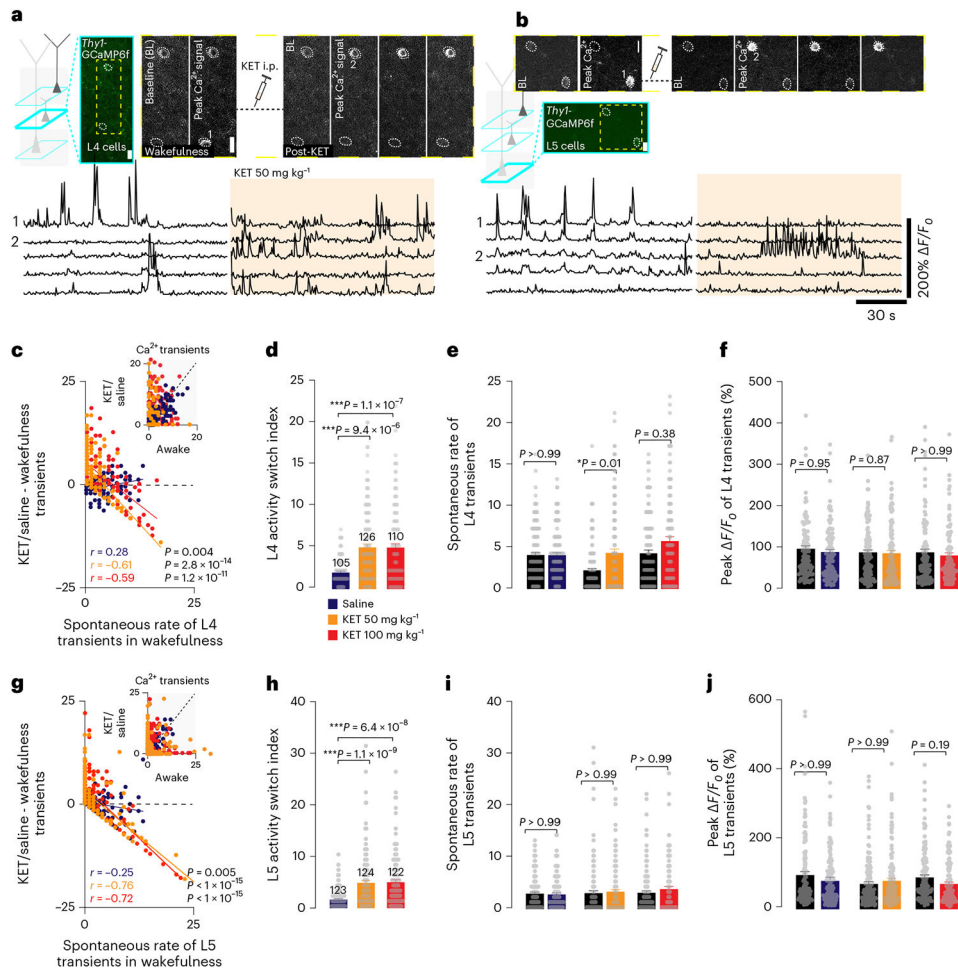
Fig. 2 |. KET induces a neuronal switch in the input and output cortical layers of S1.
a,b, Two-photon images (top) and GcaMP6 traces (bottom) of individual L4 (**a**) and L5
(**b**) neurons before and after KET 50 mg kg^{-1} in *Thy1*-GCaMP6f. Top: Representative
cortical regions (teal box) and cropped region (yellow dashed box) show two cells. Cell
1 in both L4 and L5 is spontaneously active under wakefulness, which inactivates under
KET 50 mg kg^{-1}, and vice versa for cell 2. Multiple peak *F/F*$_0$ images (3) during KET
state are shown. KET-induced switch was observed in all imaged mice stemming from >3
litters. Scale bar, 20 μm. Bottom: representative GCaMP6 traces of individual neurons under
wakefulness/KET 50 mg kg^{-1}. **c,g**, Difference in calcium transients induced by KET or
saline from baseline wakefulness versus wakefulness activity in L4 (**c**) and L5 (**g**) neurons.
Note the strong negative correlation (linear fit) between wakefulness activity and KET in
L4 (Pearson correlation KET 50 mg kg^{-1}: $r = -0.61$, $P = 2.8 \times 10^{-14}$; 100 mg kg^{-1}: $r = -0.59$, $P = 1.2 \times 10^{-11}$) and L5 (KET 50 mg kg^{-1}: $r = -0.76$, $P < 1 \times 10^{-15}$; 100 mg kg^{-1}:
$r = -0.72$, $P < 1 \times 10^{-15}$). Subplot in upper right shows the number of transients in the
wakefulness versus saline or KET. **d,h**, ASI across saline-injected mice (L4: 105 neurons
from nine mice; L5: 123 neurons from nine mice) and KET-injected mice in L4 (**d**; KET 50
mg kg^{-1}: 126 neurons from seven mice; 100 mg kg^{-1}: 110 neurons from eight mice) and
L5 (**h**; KET 50 mg kg^{-1}: 124 neurons from seven mice; 100 mg kg^{-1}: 122 neurons from

seven mice) neurons. L4 KET 50/100 mg kg^{-1}: $5.1 \pm 0.4 / 5.1 \pm 0.5$ versus saline: 2.0 ± 0.2, Kruskal–Wallis: $P = 1.1 \times 10^{-7}$ and $P = 9.4 \times 10^{-6}$ respectively; L5 KET 50/100 mg kg^{-1}: $4.9 \pm 0.5/5.0 \pm 0.5$ versus saline: 1.7 ± 0.2, Kruskal–Wallis: $P = 6.4 \times 10^{-8}$ and $P = 1.1 \times 10^{-9}$ respectively. **e,i**, Average spontaneous rate of calcium transients in L4 (**e**) and L5 (**i**) neurons under KET-injected and saline-injected mice. Kruskal–Wallis: L4, $P = 0.01$ for 50 mg kg^{-1} and L5, $P > 0.05$ for 50 mg kg^{-1} and 100 mg kg^{-1}. **f,j** Peak F/F_0 in L4 and L5 neurons under KET-injected and saline-injected mice. Kruskal–Wallis: L4 and L5, $P > 0.05$ for 50 mg kg^{-1} and 100 mg kg^{-1}. Same cells italicized in **d,h** are presented in **c,e,f** (L4) and **g,i,j** (L5), respectively. Both Kruskal–Wallis and Pearson correlation one-sided. Error bars show s.e.m. ***$P < 0.05$, **$P < 0.01$ and ***$P < 0.001$. BL, baseline.
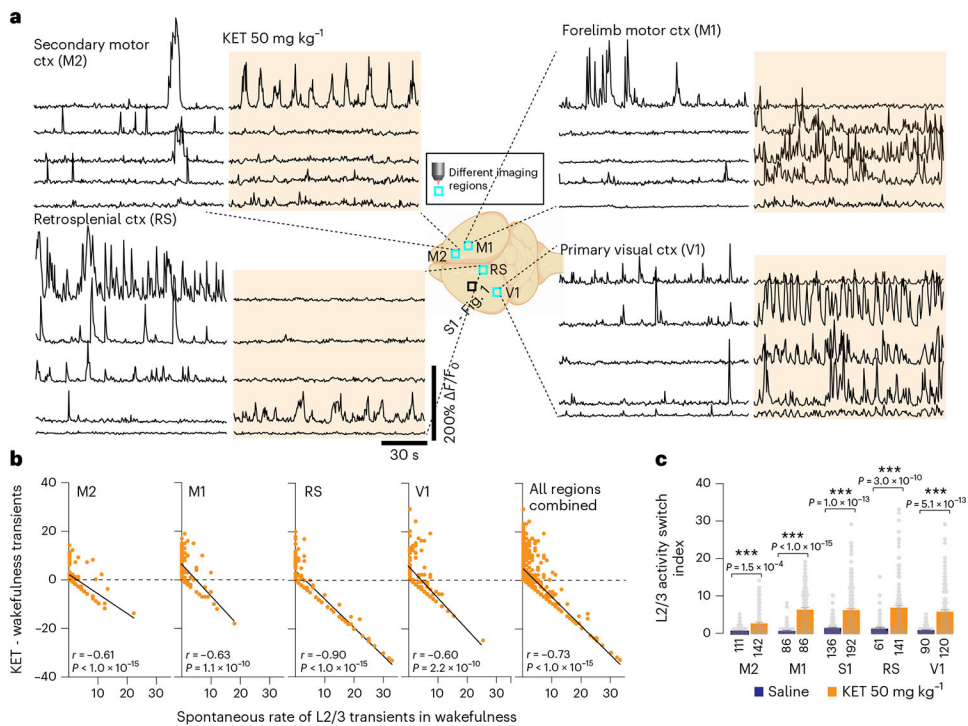
Fig. 3 |. KET induces widespread reorganization of L2/3 activity across the neocortex.

a, Cartoon of mouse brain in center of panel demarcates imaging locations (teal boxes) across neocortex. Surrounding traces of L2/3 neurons from these regions under wakefulness and KET at 50 mg kg^{-1}. Responses to KET 100 mg kg^{-1} in Extended Data Fig. 6. Representative traces carried out on at least three animals per group. **b**, Strong negative correlations between L2/3 activity in wakefulness versus after KET administration exist in all imaging regions: M2 (one-sided Pearson correlation: $r = -0.61$, $P < 1 \times 10^{-15}$); M1 ($r = -0.63$, $P = 1.1 \times 10^{-10}$); RS ($r = -0.90$, $P < 1 \times 10^{-15}$); and V1 ($r = -0.60$, $P = 2.2 \times 10^{-10}$). All regions imaged (490 neurons from 14 mice) under KET 50 mg kg^{-1} yielded significant negative correlation with wakefulness activity ($r = -0.73$, $P < 1 \times 10^{-15}$). **c**, ASI in saline-injected (M2: 136 neurons from three mice; M1: 86 neurons from three mice; RS: 61 neurons from three mice; V1: 90 neurons from four mice) and KET-injected mice in L2/3 (M2: 143 neurons from five mice; M1: 86 neurons from three mice; RS: 141 neurons from three mice; V1: 120 neurons from three mice). M2: KET 50 mg kg^{-1}: 2.9 ± 0.3 versus saline: 0.8 ± 0.1; M1: KET 50 mg kg^{-1}: 6.5 ± 0.6 versus saline: 0.8 ± 0.2; RS: KET 50 mg kg^{-1}: 7.0 ± 0.6 versus saline: 1.5 ± 0.4; V1: KET 50 mg kg^{-1}: 6.0 ± 0.5 versus saline: 1.1 ± 0.1; one-sided Kruskal–Wallis, $P < 0.001$, with Dunn's multiple comparisons with saline-injected mice, P values: M2 $= 1.5 \times 10^{-4}$, M1 $< 1.0 \times 10^{-15}$, S1 $= 1.0 \times 10^{-13}$, RS $= 3.0 \times 10^{-10}$, V1 $= 5.1 \times 10^{-13}$. Error bars show s.e.m. ***$P < 0.001$. ctx, cortex.
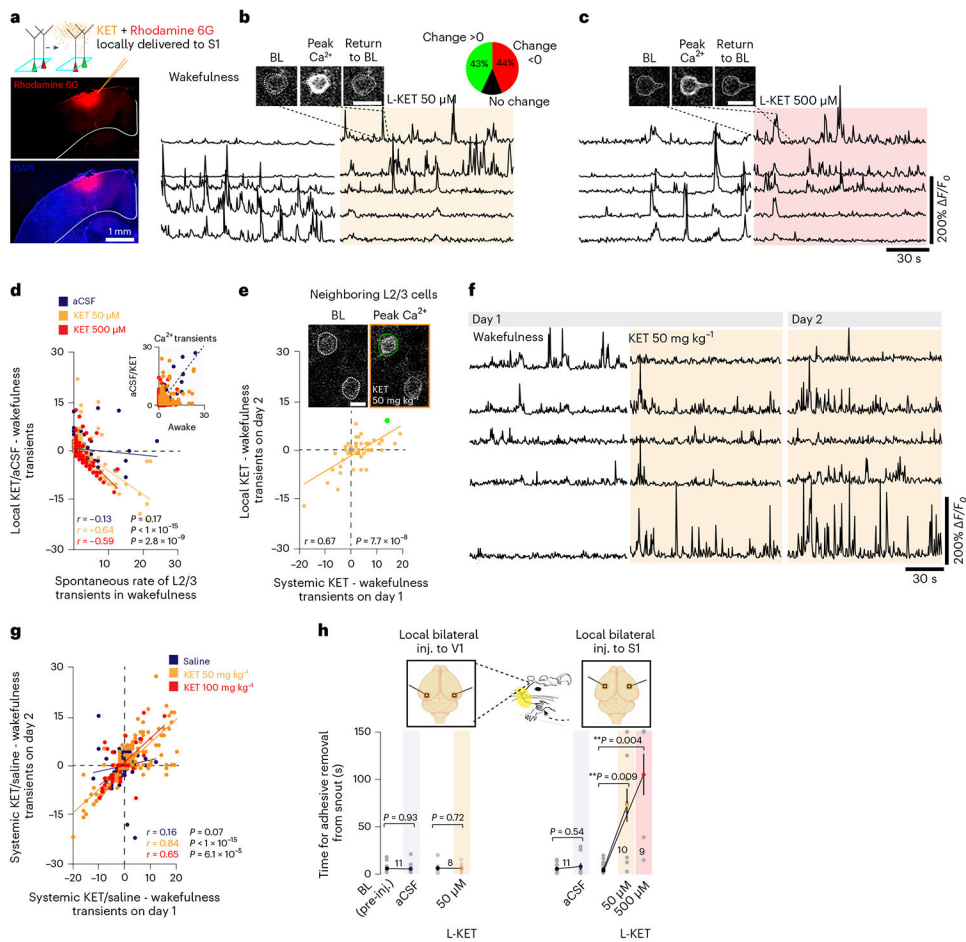
Fig. 4 |. Local KET delivery in S1 induces a neuronal switch in the active population of L2/3 neurons.

a, Confocal image of S1 after pressure application of KET mixed with Rhodamine 6G to the superficial cortex. **b,c**, Representative traces of L2/3 neurons under wakefulness and local (L-) KET at 50 μM and 500 μM to S1. Two-photon images show the rise and fall of GCaMP6f signal during a single transient in the presence of L-KET. Pie graph (upper right in **b**) shows the proportion of L2/3 neurons with increasing, decreasing and stable changes in activity under L-KET at 50 μM. **d**, Difference in calcium transients induced by L-KET or aCSF from baseline wakefulness versus wakefulness activity in L2/3 neurons (50 μM: Pearson correlation: $r = -0.64$, $P < 1 \times 10^{-15}$, 157 neurons from four mice; 500 μM: $r = -0.59$, $P = 2.8 \times 10^{-9}$, 84 neurons from four mice). aCSF injection did not significantly alter L2/3 neuronal activity from baseline wakefulness ($r = -0.13$, $P = 0.17$, 116 neurons from three mice). **e**, Activity of systemic KET 50 mg kg^{-1} was positively correlated with L-KET in S1 L2/3 neurons (Pearson correlation: $r = 0.67$, $P = 7.7 \times 10^{-8}$, 51 neurons from three mice). Inset of neighboring L2/3 neurons where KET activates one cell (teal) but not the other (gray). **f**, Representative traces of L2/3 pyramidal neurons recorded during wakefulness and then after KET 50 mg kg^{-1} over 2 days. **g**, Repetitive systemic dosing of KET (day 1 versus day 2), but not saline, modulated the S1 L2/3 similarly (KET 50 mg kg^{-1}: Pearson correlation: $r = 0.84$, $P < 1 \times 10^{-15}$, 185 neurons from five mice; 100 mg

kg^{-1}: $r = 0.65$, $P = 6.1 \times 10^{-5}$, 32 neurons from two mice versus saline: $r = 0.16$, $P = 0.07$, 134 neurons from four mice). **h**, Time for adhesive removal from snout before and after local delivery of KET/aCSF (orange/gray circles, respectively; single circle signifies individual animal) to either bilateral S1 or V1. KET at both 50 μM and 500 μM (Wilcoxon rank-sum test, $P < 0.01$) to S1 induced an impairment in performance but not when delivered to V1 ($P > 0.05$). Representative images and traces carried out on at least three animals per group except for **e** in KET 100 mg kg^{-1} condition (two mice). n for animals are italicized in **h**. Scale bar, 20 μm. Wilcoxon rank two-sided and Pearson correlation one-sided. Error bars show s.e.m. *$P < 0.05$, **$P < 0.01$ and ***$P < 0.001$. BL, baseline.
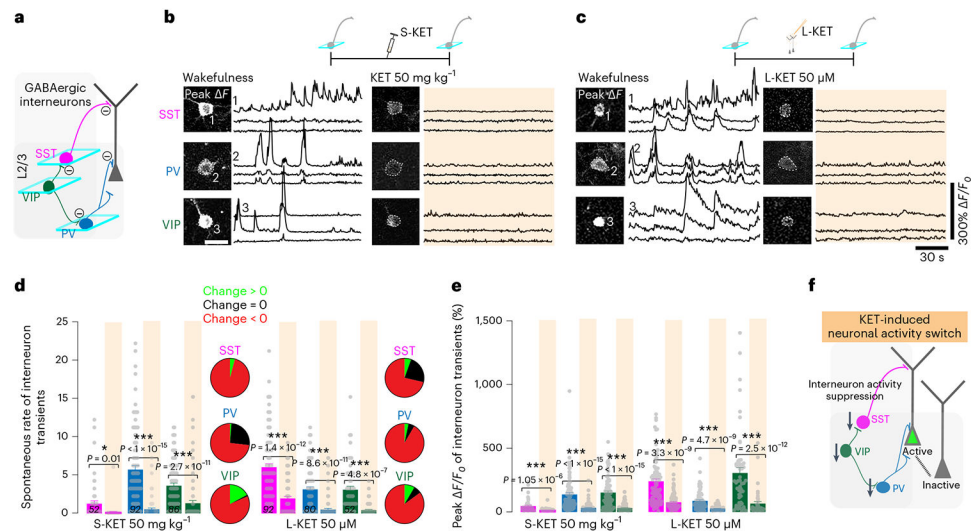
Fig. 5 |. Systemic and local KET suppresses activity in S1 interneuron subtypes.
a, Schematic of cortical interneurons and their understood connectivity to neighboring interneurons and pyramidal neuron. Interneuron-mediated inhibition denoted by axon with circled negative sign at terminal. Imaging of specific interneuron subtypes highlighted by teal boxes. **b,c**, Top: cartoon depiction of interneuron imaging experiment for systemic KET (S-KET) at 50 mg kg^{-1} (**b**) and local KET (L-KET) (**c**) at 50 μM. Bottom: representative two-photon images and GCaMP6 traces of spontaneous activity of each interneuron subtype in wakefulness and after KET administration. Images show baseline and peak GCaMP6f signal for traces with corresponding number. Scale bar, 20 μm. **d,e**, Comparison between spontaneous rate of activity (**d**) and peak signals (**e**) across interneurons subtypes in S1 after S-KET or L-KET (cell numbers italicized in bottom portion of graph for both doses; 17 mice and ten mice across various lines at S-KET and L-KET, respectively). Pie graphs, displayed in **d**, show the portion of cells increasing/decreasing/no change in activities after KET administration for each interneuron subtypes. Note the strong reduction of spontaneous interneuron activity and peak signals with both KET doses (one-sided Kruskal–Wallis, $P < 0.001$ followed by Dunn's multiple comparisons for **d:** $P < 0.05$ for SST/S-KET and $P < 0.001$ for all other comparisons; **e:** $P < 0.001$ for all comparisons; exact P values in figure). Representative images and traces carried out on at least three animals per group. **f**, Schematic from **a** highlighting that KET-induced suppression of GABAergic interneuron activity may promote an activity switch in L2/3 pyramidal neurons. Error bars show s.e.m. $*P < 0.05$ and $***P < 0.001$.
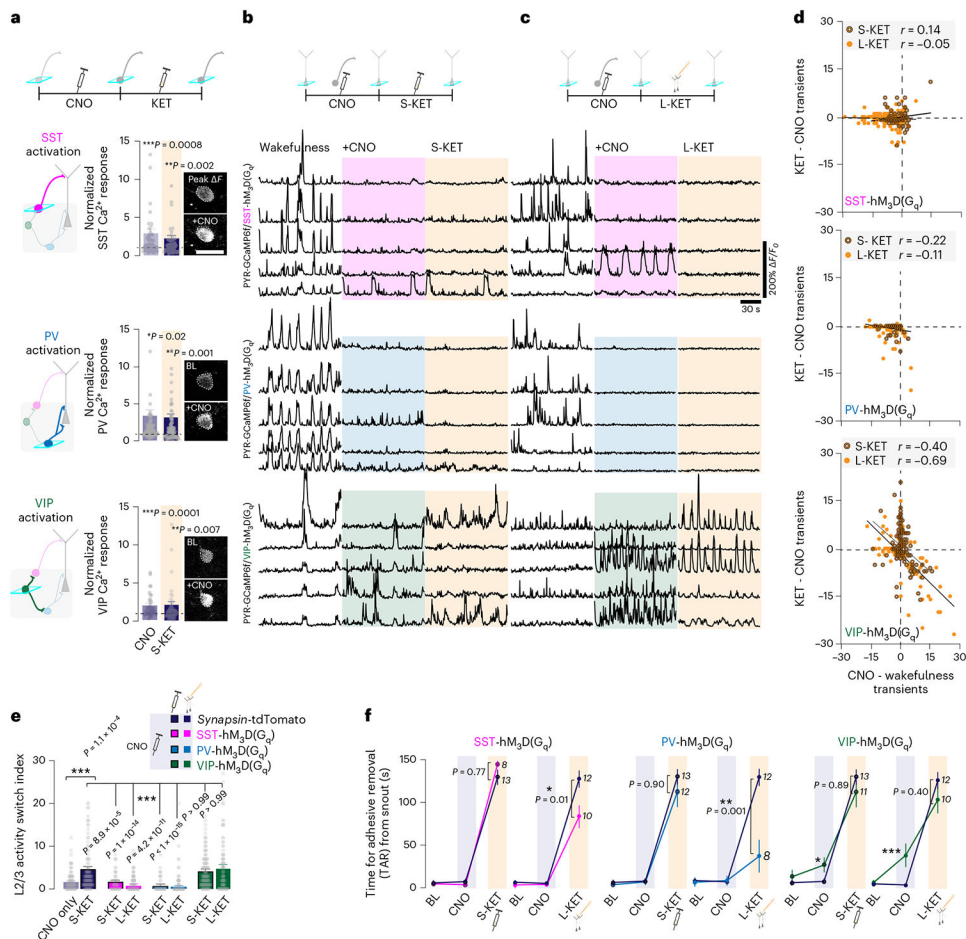
Fig. 6 |. KET-induced suppression of SST or PV interneurons is necessary for the activity switch in L2/3 pyramidal neurons.

a, Experimental timeline (top) of DREADD-induced activation of interneuron subtypes (bottom). Interneuron subtypes expressing DREADD hM3D(Gq)-mCherry and their responses to CNO (light blue) followed by systemic KET (S-KET) (navy) (SST: 47 cells from four mice; PV: 84 cells from five mice; VIP: 37 cells from three mice). In each interneuron subtype, CNO induced a doubling of calcium activity, and this was not affected by KET (two-sided paired Student's *t*-test, $P < 0.05$ for all). Two-photon images show the baseline and peak GCaMP6f signal after CNO in different interneuron subtypes. Scale bar, 20 μm. **b,c**, Experimental timeline (top) and representative traces of L2/3 pyramidal cells under wakefulness, CNO and then S-KET (**b**) or local KET (L-KET) (**c**). PV and SST activation both suppress L2/3 pyramidal activity. VIP cell activation maintained L2/3 cells activity through CNO and KET treatment. **d**, L2/3 cell activity in the setting of CNO-induced interneuron activation versus its response to S-KET and L-KET. SST (one-sided Pearson correlation: S-KET: $r = 0.14$, $P = 0.27$, 65 neurons from three mice; L-KET: $r = -0.05$, $P = 0.52$, 173 neurons from five mice) or PV (S-KET: $r = -0.22$, $P = 0.13$, 51 neurons from three mice; L-KET: $r = -0.11$, $P = 0.14$, 178 neurons from five mice) activation prevented KET's neuronal switch, whereas VIP activation (S-KET: $r = -0.40$, $P = 1.9 \times 10^{-6}$, 133 neurons from four mice; L-KET: $r = -0.69$, $P = 2 \times 10^{-14}$, 95 neurons from

three mice) enabled KET's neuronal switch in L2/3 pyramidal neurons. **e**, S-KET-induced and L-KET-induced L2/3 ASI after chemogenetic activation of interneuron subtypes. One-sided Kruskal–Wallis, $P < 0.001$ followed by Dunn's multiple comparison: $P < 0.001$ for both SST and PV groups, $P > 0.99$ for VIP groups. **f**, TAR measured across baseline (BL) wakefulness, CNO and KET, for both S-KET (left) and L-KET (right). Left: S-KET administration after interneuron subtype activation significantly impaired performance on TAR (pink-SST/blue-PV/green-VIP lines) to levels no different than S-KET administration in control mice expressing AAV-*synapsin*-tdTomato (navy lines) (two-sided Mann–Whitney, $P > 0.05$ for all subtypes). Right: The L-KET-induced impairment in TAR performance (navy lines) was reduced by prior CNO activation of either SST or PV interneurons but not VIP interneurons (colored lines) (two-sided Mann–Whitney, $P < 0.05$ for SST and $P < 0.01$ for PV). *n* for animals are italicized next to treatment condition. Exact *P* values for **e** and **f** are in the figure. Error bars show s.e.m. *$P < 0.05$, **$P < 0.01$ and ***$P < 0.001$. BL, baseline.
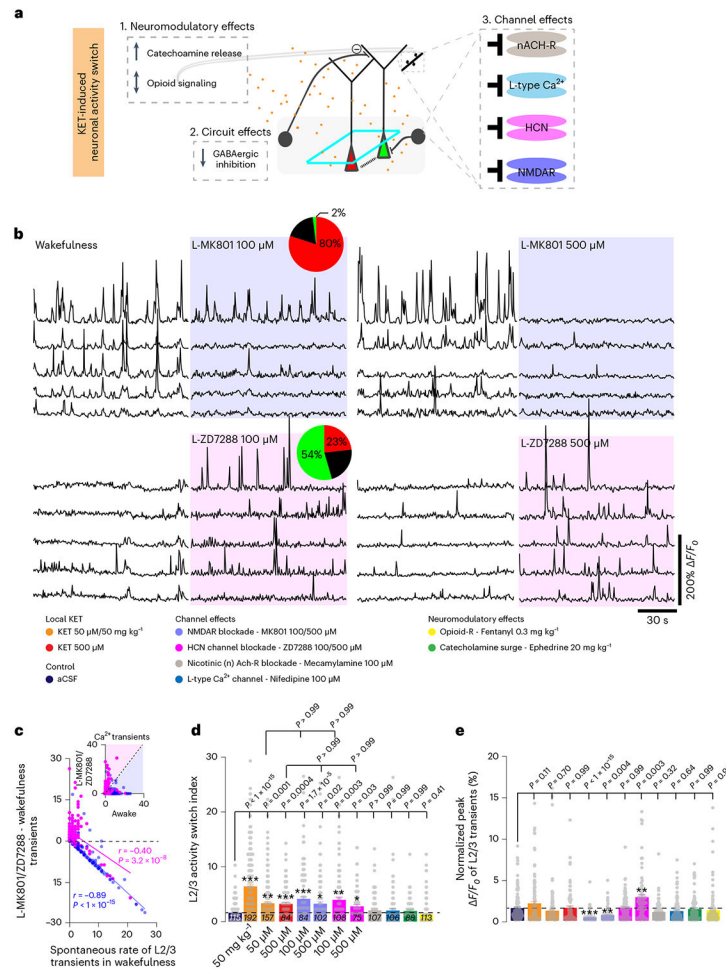
Fig. 7 |. Inhibition of NMDARs or HCN channels drives a neuronal activity switch.
a, Cartoon depicting the multiple effects potentially engaged by KET in cortical circuits. Figure 5 demonstrates the KET-associated reduction in cortical inhibition. **b**, Representative traces of L2/3 neurons under wakefulness and local (L-) MK801 at 100 μM (top traces; 122 neurons from four mice) and 500 μM (102 neurons from five mice), L-ZD7288 at 100 μM (bottom traces; 108 neurons from three mice) and 500 μM (75 neurons from three mice). Pie graphs show the proportion of L2/3 neurons with increasing, decreasing and stable changes in activity under L-MK801 and L-ZD7288 at 100 μM. **c**, Difference in calcium transients induced by L-MK801 (one-sided Pearson correlation: $r = -0.89$, $P < 1 \times 10^{-15}$) or L-ZD7288 ($r = -0.40$, $P = 3.2 \times 10^{-8}$) from baseline wakefulness versus wakefulness activity. Subplot in upper right shows the number of transients in the wakefulness versus L-MK801 and L-ZD7288. **d,e**, ASI (**d**) and peak responses (**e**) across local drug delivery experiments. Note the significant increase in ASI for L-KET, L-MK801 and L-ZD7288 (one-sided Kruskal–Wallis, $P < 0.001$ followed by Dunn's multiple comparison: L-MK801, $P < 0.05$ for both concentrations; L-ZD7288, $P < 0.05$ for both concentrations), whereas other KET molecular targets were ineffective inducers of an activity switch in L2/3 neurons at concentrations tested (mecamylamine, $P > 0.99$ (107 neurons from three mice); nifedipine, $P > 0.99$ (106 neurons from three mice); fentanyl, $P = 0.41$ (113 neurons from

three mice); ephedrine, $P > 0.99$ (88 neurons from three mice)). Exact P values for **d,e** are in the figure. Error bars show s.e.m. *$P < 0.05$, **$P < 0.01$ and ***$P < 0.001$.
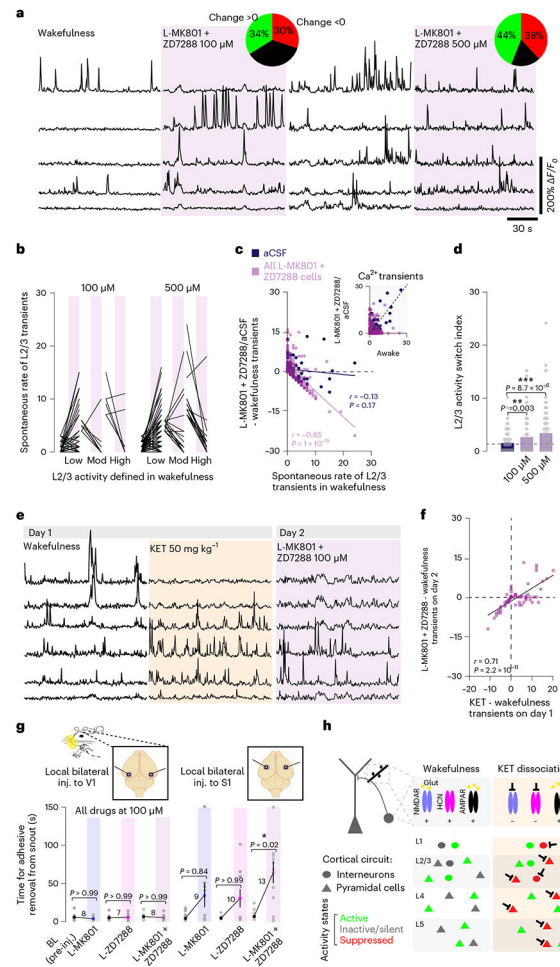
Fig. 8 |. Combined inhibition of NMDARs and HCN channels recapitulates the effects of KET administration.

a, Representative traces of L2/3 neurons under wakefulness and combined L-MK801 + ZD7288 at 100 μM or 500 μM. Pie graphs show the proportion of L2/3 neurons with increasing/decreasing/no change in activity under combined blocker conditions. **b**, Line scatter plots of individual L2/3 cell activity before and after combined L-MK801 + ZD7288. Low/moderate/ high activity bins defined in drug-free wakefulness. **c**, Difference in calcium transients induced by combined L-MK801 + ZD7288 (both concentrations plotted together) or aCSF from baseline wakefulness versus wakefulness activity. Note the strong negative correlation between activity in wakefulness and combined L-MK801 + ZD7288 (Pearson correlation: $r = -0.65$, $P < 1 \times 10^{-15}$) versus aCSF ($r = -0.13$, $P = 0.17$). Subplot in upper right shows the number of transients in the wakefulness versus combined L-MK801 + ZD7288. **d**, ASI for combined blocker delivery (Kruskal–Wallis, $P < 0.001$ followed by Dunn's multiple comparison: $P < 0.01$ for both concentrations; $n = 89$ neurons from three mice for 100 μM and $n = 152$ neurons from four mice for 500 μM). **e**, Representative traces of L2/3 neurons under wakefulness, KET at 50 mg kg^{-1} and then on the following day with combined blockers (100 μM, 66 neurons from three mice). **f**, L2/3 activity induced by systemic KET at 50 mg kg^{-1} versus combined blockers (one-sided Pearson correlation: $r = 0.71$, $P = 2.2 \times 10^{-11}$). **g**, AR test before and after the local delivery of L-MK801, L-ZD7288

or combined blockers to bilateral S1 (one-sided Kruskal–Wallis, $P < 0.001$ followed by Dunn's multiple comparison: $P = 0.02$ for L-MK801 + ZD7288, $P > 0.05$ for individual blockers) and V1 ($P > 0.99$ for all). **h**, Cartoon of molecular, cellular and circuit changes in neocortex underlying the non-ordinary brain state triggered by KET. In wakefulness (left), a network of active cells (green) that are mostly driven by glutamatergic receptor activation, both AMPAR and NMDAR, and modulated by HCN1 activity. Under KET (right), NMDAR conductances are inhibited by KET (black inhibitory arrows) transitioning previously active cells into a low-firing mode (green cells turned red). Neighboring neurons, in the setting of reduced GABAergic inhibitory tone and HCN inhibition, efficiently summate a new set of KET-driven inputs/synaptic responses, yielding activation (new set of green cells). The shift away from an NMDAR predominant neurotransmission to AMPAR and a change in inputs drive the neuronal activity of a different network of neurons, creating a new unique pattern of KET-dependent circuit activity across the cortical mantle, contributing to KET's disconnected state. Exact P values for **d,g** are in the figure. Error bars show s.e.m. *$P < 0.05$, **$P < 0.01$ and ***$P < 0.001$. BL, baseline.